

Interaction dependence of the Hall response for the Bose-Hubbard triangular ladder

Catalin-Mihai Halati¹ and Thierry Giamarchi¹

¹*Department of Quantum Matter Physics, University of Geneva, Quai Ernest-Ansermet 24, 1211 Geneva, Switzerland*
(Dated: September 24, 2024)

We explore the behavior of the Hall response of a Bose-Hubbard triangular ladder in a magnetic field as a function of the repulsive on-site atomic interactions. We consider a wide range of interaction strengths, from the weakly interacting limit to the hardcore regime. This is realized by computing the Hall polarization following the quench of a weak linear potential which induces the flow of a current through the system, using time-dependent matrix product state numerical simulations. We complement our understanding in the regime of small magnetic fields by analytical calculations of the equilibrium value of the Hall polarization for non-interacting bosonic atoms, or under a mean-field assumption. The Bose-Hubbard triangular flux ladder exhibits a rich phase diagram, containing Meissner, vortex and biased-chiral superfluid phases. We show that the Hall response can be employed to fingerprint the various chiral state, the frustration effects occurring in the limit of strong interactions, and the phase boundaries of the equilibrium phase diagram.

I. INTRODUCTION

Strongly correlated topological matter exhibits exotic properties like particles with fractional quantum numbers and anyonic exchange statistics, which offer a promising avenue for quantum computing applications [1, 2]. One of the paradigmatic example of topological quantum states is the fractional quantum Hall state [3–5], stemming from the interplay of strong interactions and magnetic fields. The realization of such topological non-trivial states has been an important goal for ultracold atoms platforms. As in these systems the atoms are neutral the magnetic fields are artificially realized, e.g. by coupling to laser light via Raman processes [6–8]. This technique lead to the experimental realization of the artificial magnetic fields for atoms confined to quasi-one-dimensional ladders, or two-dimensional geometries systems, for both bosonic and fermionic atomic species [9–19]. Furthermore, recently a Laughlin-type fractional quantum Hall state of two-atoms has been prepared [20].

One of the central questions in the field is related to the design of experimentally relevant probes that can unravel the non-trivial topological properties of the prepared quantum states. In solid state materials, the Hall effect, i.e. monitoring the induced transverse current upon the application of a force, has been a widely employed transport measurement. More recently, the Hall response has also accessible for ultracold atoms in optical lattice and for weakly interacting gases has been measured from the center-of-mass drifts or local currents [14, 17, 18]. Furthermore, theoretical proposals relate the quantized Hall response to topological invariants for small interacting ensembles for identifying the fractional states [21, 22]. However, a complete understanding of the behavior of the Hall response when strong interactions are present is still lacking. Theoretical progress is being made in the case of ladder systems [23–28], the minimal setups for the study of the interplay of interactions and orbital effects, or making use of special geometries [29–31]. In particular, the theoretical prediction of an universal Hall

response occurring for certain parameters for interacting fermionic ladders [25] has been experimentally confirmed [19]. For the case of ladders a universal relation between the Hall resistance and the charge stiffness has also been proposed [27].

In this work, we explore the Hall response for a Bose-Hubbard triangular ladder under the action of a magnetic field, focusing on the behavior of the Hall polarization for a wide range of on-site atomic interactions. This is motivated by recent studies which showed that the Hall response can be employed as a sensitive probe for the features of the underlying phase diagram, either in the case of hardcore bosons in the triangular geometry [28], or in the limit of small magnetic fields for square ladders [27]. Furthermore, the triangular flux ladders have proven to exhibit rich phase diagrams [32–44], with frustration-induced effects and phases without an equivalent in the unfrustrated square geometry [40].

The plan of the paper is as in the following, in Sec. II we describe the model we investigate and the protocol employed for the numerical calculation of the Hall polarization. In Sec. III we briefly present the numerical method based on matrix product states employed in this work, while in Sec. IV we perform analytical calculations in the non-interacting and mean-field limits for computing the equilibrium Hall polarization. The results are presented in Sec. V, focusing first on the behavior in the Meissner superfluid phase, Sec. VA, followed by an analysis around the phase transitions boundaries, Sec. VB, in the biased-chiral superfluid phase, Sec. VC, and finalizing by discussing the commensurability effects occurring in the vortex superfluid phase, Sec. VD. We discuss our results and conclude in Sec. VI.

II. MODEL AND PROTOCOL

We consider interacting bosonic atoms confined to a triangular ladder under the action of a magnetic field, as sketched in Fig. 1. The Hamiltonian of the Bose-Hubbard

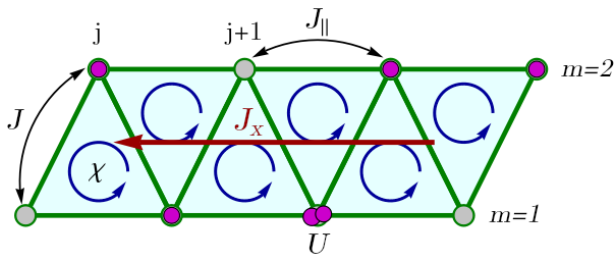


FIG. 1: Sketch of the triangular flux ladder model. The legs are denoted by $m = 1, 2$ and the sites on each leg numbered by j . The bosonic atoms can tunnel along the rungs with amplitude J and along the legs with amplitude J_{\parallel} . We take into account repulsive on-site interaction between the atoms of strength U , and a flux χ pierces each triangular plaquette. Due to the presence of a linear potential V_x a current \mathbf{J}_x passes through the ladder.

model in a magnetic field is given by [40]

$$\begin{aligned}
 H &= H_{\parallel} + H_{\perp} + H_{\text{int}}, \\
 H_{\parallel} &= -J_{\parallel} \sum_{j=1}^{L-1} \left(e^{-i\chi} b_{j,1}^{\dagger} b_{j+1,1} + \text{H.c.} \right) \\
 &\quad - J_{\parallel} \sum_{j=1}^{L-1} \left(e^{i\chi} b_{j,2}^{\dagger} b_{j+1,2} + \text{H.c.} \right), \\
 H_{\perp} &= -J \sum_{j=1}^L \left(b_{j,1}^{\dagger} b_{j,2} + \text{H.c.} \right) \\
 &\quad - J \sum_{j=1}^{L-1} \left(b_{j+1,1}^{\dagger} b_{j,2} + \text{H.c.} \right), \\
 H_{\text{int}} &= \frac{U}{2} \sum_{j=1}^L \sum_{m=1}^2 n_{j,m} (n_{j,m} - 1).
 \end{aligned} \tag{1}$$

We denote by $b_{j,m}$ and $b_{j,m}^{\dagger}$ the bosonic annihilation and creation operators at position j and leg $m = 1, 2$. $\rho = N/(2L)$ represents the atomic filling, with the total number of particles $N = \sum_{j=1}^L \sum_{m=1}^2 n_{j,m}$ and L the number of sites on each leg of the ladder. H_{\parallel} gives the tunneling along the two legs of the ladder, with amplitude J_{\parallel} . The complex value of the tunneling amplitude stems from the presence of a magnetic field, with strength characterized by the flux χ [6, 7]. The tunneling along the rungs of the ladder is described by H_{\perp} with amplitude J . The atoms interact repulsively if on the same lattice site, with the interaction strength $U > 0$. We assume $\hbar = 1$ in the following. This model has a rich phase diagram of chiral quantum phases, as discussed in Ref. [28, 40], we give an overview of the phase diagrams for the considered parameter regimes in Sec. V.

We are interested in the Hall response of the system and its dependence on the on-site interaction strength for the different phases present. To realize this we monitor the dynamics of the system following the quench of a

linear potential in the x -direction

$$V_x = \mu \sum_{j=1}^L \sum_{m=1}^2 \left[j + \frac{1}{2}(m-1) \right] n_{j,m}. \tag{2}$$

This protocol has been investigated for square ladders in Refs. [25, 26] and we analyzed it for the triangular ladder in the limit of hardcore interactions in Ref. [28]. Furthermore, it has been experimentally implemented for interacting fermionic atoms on a square ladder in Ref. [19]. In order to compute the Hall response, we begin with the system in its ground state at time $tJ = 0$. Following the quench with the potential V_x at $t > 0$ a total current, \mathbf{J}_x , is present in the x -direction and, due to the presence of the magnetic flux, between the two legs of the ladder a density imbalance, P_y , develops. These observables are defined for the triangular ladder as

$$\begin{aligned}
 P_y &= \sum_j (n_{j,1} - n_{j,2}), \\
 \mathbf{J}_x &= -i \sum_j \left[\frac{J}{2} \left(b_{j,1}^{\dagger} b_{j,2} + b_{j,2}^{\dagger} b_{j+1,1} - \text{H.c.} \right) \right. \\
 &\quad \left. + J_{\parallel} \left(e^{-i\chi} b_{j,1}^{\dagger} b_{j+1,1} + e^{i\chi} b_{j,2}^{\dagger} b_{j+1,2} - \text{H.c.} \right) \right],
 \end{aligned} \tag{3}$$

where in the current \mathbf{J}_x we have contributions from the two legs of the ladder and also from the rungs due to the triangular geometry, for its derivation see Refs. [28, 45]. A current flowing towards smaller values of the index j corresponds to negative values of \mathbf{J}_x .

The Hall response of the system is quantified by the Hall polarization, defined as the ratio of the two observables defined in Eq. (3) [25, 26]

$$P_H(t) = \frac{\langle P_y \rangle(t)}{\langle \mathbf{J}_x \rangle(t)/J}. \tag{4}$$

In the numerator we usually consider the imbalance difference with respect to the ground state value, $\langle P_y \rangle(t) - \langle P_y \rangle(0)$, as phases like the biased-chiral superfluid exhibit a finite value of the imbalance in equilibrium.

The usefulness of employing the Hall polarization as a measure of the response stems from the fact that even though the magnitudes of the density imbalance and total current grow under the action of the linear potential, $P_H(t)$ stabilizes to a transient steady value at intermediate times [25, 26, 28]. We compute $P_H(t)$ numerically using time-dependent matrix product states methods as described in Sec. III and its equilibrium value analytically in the non-interacting or mean-field limits in Sec. IV. The steady value of the Hall polarization we denote by $\langle\langle P_H \rangle\rangle$, where we performed the average over $P_H(t)$ for a time interval of at least $10/J$. We work in a regime of small values of the linear potential μ/J , such that the results shown are independent on its value. However, if we decrease the value of the potential we have access to longer times in the dynamics before the finite size effects become relevant. We note that we discussed the influence of μ/J in more details for the hardcore case in the Supplemental Material of Ref. [28]

III. MATRIX PRODUCT STATES NUMERICAL METHODS

In the following, we briefly describe the numerical approaches used in this work. To numerically obtain the ground state of the Hamiltonian H , Eq. (1), we employed a finite-size density matrix renormalization group (DMRG) algorithm in the matrix product state (MPS) representation [46–50], implemented using the ITensor Library [51]. We consider ladders with a number of sites on each leg of $L = 60$ and $L = 90$, and with a maximal bond dimension up to 500, ensuring that the truncation error is at most 10^{-10} . Since we are considering a bosonic model with finite interactions the local Hilbert space is large, thus, a cutoff for its dimension is needed. We use a maximal local dimension of at least four or five states per site, depending on the value of the interactions.

The time evolution with the additional potential $H + V_x$, Eq. (2), is performed using the time-dependent matrix product state method (tMPS) based on Trotter-Suzuki decomposition [48, 52, 53]. The convergence was ensured with a time step of $dtJ/\hbar = 0.01$ and the measurements were performed every tenth time step. We maintain the same bond dimension as for the ground state search, this ensures that up to the times considered in this work, the truncation error is at most 10^{-9} .

IV. ANALYTICAL CALCULATION OF THE EQUILIBRIUM HALL POLARIZATION

In Refs. [25, 26] it was shown that the transient steady value $\langle\langle P_H \rangle\rangle$ agrees with the equilibrium Hall polarization obtained for periodic boundary conditions upon the threading of a flux through the system. In the following, we derive the equilibrium value analytically for the non-interacting case for small values of the flux χ and using a mean-field approach in the Meissner phase.

The Hamiltonian of the system for periodic boundary conditions in the x -direction, upon the threading of a flux $\tilde{\Phi}$ through the cylinder and under the action of a potential difference between the two legs of the ladder is

given by

$$\begin{aligned} \tilde{H} = & -J_{\parallel} \sum_{j=1}^L \left(e^{-i\chi - i\tilde{\Phi}/L} b_{j,1}^{\dagger} b_{j+1,1} + \text{H.c.} \right) \\ & - J_{\parallel} \sum_{j=1}^L \left(e^{i\chi - i\tilde{\Phi}/L} b_{j,2}^{\dagger} b_{j+1,2} + \text{H.c.} \right) \\ & - J \sum_{j=1}^L \left(e^{-i\tilde{\Phi}/2L} b_{j,1}^{\dagger} b_{j,2} + e^{i\tilde{\Phi}/2L} b_{j+1,1}^{\dagger} b_{j,2} + \text{H.c.} \right) \\ & + \frac{U}{2} \sum_{j=1}^L \sum_{m=1}^2 n_{j,m} (n_{j,m} - 1) \\ & + E_y \sum_{j=1}^L (n_{j,1} - n_{j,2}), \end{aligned} \quad (5)$$

where E_y is the energy difference between the two legs of the ladder. The Hall polarization can be derived in terms of the ground state energy derivatives [23–25]. In this sense, following the notations of Ref. [25], we expand the ground state energy $\mathcal{E}_0(\Phi, \chi, E_y)$ to the third order in Φ, χ, E_y around zero

$$\begin{aligned} \mathcal{E}_0(\tilde{\Phi}, \chi, E_y) = & \mathcal{E}_0(0, 0, 0) + \frac{\tilde{\Phi}^2}{2} \frac{\partial^2 \mathcal{E}_0}{\partial \tilde{\Phi}^2} + \frac{\chi^2}{2} \frac{\partial^2 \mathcal{E}_0}{\partial \chi^2} \\ & + \frac{E_y^2}{2} \frac{\partial^2 \mathcal{E}_0}{\partial E_y^2} + \tilde{\Phi} \chi E_y \frac{\partial^3 \mathcal{E}_0}{\partial \tilde{\Phi} \partial \chi \partial E_y}, \end{aligned} \quad (6)$$

where we considered only the terms that do not vanish due to symmetries. The current and density imbalance can be computed as derivatives of the energy as

$$\langle \mathbf{J}_x \rangle^{\text{eq}} = L \frac{\partial \mathcal{E}_0}{\partial \tilde{\Phi}}, \quad \langle P_y \rangle^{\text{eq}} = \frac{\partial \mathcal{E}_0}{\partial E_y}. \quad (7)$$

Around the expansion point we have

$$\begin{aligned} \langle \mathbf{J}_x \rangle^{\text{eq}} = & L \tilde{\Phi} \frac{\partial^2 \mathcal{E}_0}{\partial \tilde{\Phi}^2}, \\ \langle P_y \rangle^{\text{eq}} = & E_y \frac{\partial^2 \mathcal{E}_0}{\partial E_y^2} + \tilde{\Phi} \chi \frac{\partial^3 \mathcal{E}_0}{\partial \tilde{\Phi} \partial \chi \partial E_y}. \end{aligned} \quad (8)$$

As we do not require a finite value of E_y to compute the Hall polarization we obtain the following expression for the equilibrium value [25]

$$P_H^{\text{eq}} = \frac{\chi}{L} \frac{\partial \phi \frac{\partial^3 \mathcal{E}_0}{\partial \phi \partial \chi \partial E_y}}{\frac{\partial^2 \mathcal{E}_0}{\partial \phi^2}} \Bigg|_{\chi, \tilde{\Phi}, E_y=0}. \quad (9)$$

A. Non-interacting limit

In the non-interacting limit, $U = 0$, for the Hamiltonian in Eq. (5) we can compute the dispersion relation of

the bosonic atoms

$$E_{\pm}(k) = -2J_{\parallel} \cos\left(k + \tilde{\Phi}/L\right) \cos(\chi) \pm \left\{ 2J^2 \left[1 + \cos\left(k + \tilde{\Phi}/L\right) \right] + \left[E_y + 2J_{\parallel} \sin\left(k + \tilde{\Phi}/L\right) \sin(\chi) \right]^2 \right\}^{1/2}. \quad (10)$$

At small values of the flux χ , where Eq. (9) is valid, we are in the Meissner phase and the minimum of the lower band of the dispersion is at momentum $k = 0$ [40]. Thus, using $\mathcal{E}_0 = E_-(k = 0)$ in Eq. (9) we obtain

$$P_H^{\text{eq}, U=0} = \frac{-2(J_{\parallel}/J)\chi \cos(\chi)}{1 + 4(J_{\parallel}/J) \cos(\chi) - 4(J_{\parallel}/J)^2 \sin(\chi)^2}. \quad (11)$$

We note that even though this relation is derived only for small χ , we kept in the ground state energy the full dependence on the flux χ . We compare this expression with numerical results at small interaction strengths in Sec. V A and we find a very good agreement.

B. Mean-field approach in the Meissner phase

In the limit of large atomic fillings ρ in the Meissner phase we can approximate the bosonic operator $b_{j,m} = \sqrt{\rho + \frac{1}{2}(-1)^m \delta\rho} e^{i\phi}$. The values of $\delta\rho$ and ϕ can be computed from the minimization of the energy. Furthermore, from the approximate value of the ground state energy we can obtain the Hall polarization [25]. In this mean-field approximation the Hamiltonian \tilde{H} , Eq. (5), for $E_y = 0$ reads

$$\begin{aligned} \tilde{H} = & -2J_{\parallel}L \left[\cos\left(\chi + \tilde{\Phi}/L\right) \left(\rho - \frac{1}{2}\delta\rho\right) \right. \\ & \left. + \cos\left(\chi + \tilde{\Phi}/L\right) \left(\rho + \frac{1}{2}\delta\rho\right) \right] \\ & -4JL \cos\left(\tilde{\Phi}/2L\right) \left(\rho^2 - \frac{\delta\rho^2}{4}\right)^{1/2} \\ & +UL \left(\rho^2 - \rho + \frac{\delta\rho^2}{4}\right). \end{aligned} \quad (12)$$

The energy is minimized for a local atomic imbalance of

$$\delta\rho = \frac{4J_{\parallel}\rho \sin(\chi) \sin\left(\tilde{\Phi}/L\right)}{2J \cos\left(\tilde{\Phi}/L\right) + \rho U}. \quad (13)$$

By computing the total current as the derivative of the ground state energy, Eq. (7), and using that $\langle P_y \rangle^{\text{eq}} = L\delta\rho$, we obtain the following mean-field value of the equilibrium Hall polarization

$$P_H^{\text{eq}, \text{MF}} = \frac{-2(J_{\parallel}/J) \sin(\chi)}{1 + \frac{\rho U}{2J} + 4\frac{J_{\parallel}}{J} \cos(\chi) \left(1 + \frac{\rho U}{2J}\right) - 4\frac{J_{\parallel}^2}{J^2} \sin(\chi)^2}. \quad (14)$$

We can notice that in the limit of $\chi \rightarrow 0$ and $\rho \rightarrow 0$ it agrees with the non-interacting result $P_H^{\text{eq}, U=0}$, Eq. (9).

V. RESULTS

In the following, we present the results for the Hall polarization throughout the phase diagram of the Hamiltonian, Eq. (1). We initially focus on the filling $\rho = 0.25$, considering the dependence of $\langle\langle P_H \rangle\rangle$ as a function of both the flux χ and the tunneling amplitude J_{\parallel}/J for different values of the on-site interaction U/J . For this value of the filling we obtain the same quantum phases in the ground state of the model for all values of the interaction considered, as seen in Fig. 2, where the phase diagram is depicted for $U/J = 1$ and $U/J = 10$. This allows us to study the dependence of the Hall response within the same phase as a function of U/J .

For a filling of $\rho = 0.25$ in the phase diagram we observe three distinct quantum phases [40], as shown in Fig. 2. At small values of the flux χ , or small values of the tunneling J_{\parallel}/J , we have the *Meissner superfluid* (M-SF). The Meissner superfluid is characterized by vanishing values of currents on the rungs and by chiral currents on the legs of the ladder. For larger values of the flux χ , a phase breaks the \mathbb{Z}_2 symmetry of the ladder is present, namely the *biased chiral superfluid* (BC-SF). The ground state manifold is spanned by two states exhibiting finite values of density imbalance between the two legs of opposite signs. Increasing J_{\parallel}/J we enter the *vortex superfluid* (V-SF), characterized by finite values of the currents both on the legs and the rungs of the ladder. The current pattern determines a vortex density incommensurate with the ladder geometry, scaling linearly with the flux $\rho_v = \chi/\pi$. Furthermore, at large values of the interaction strength, for certain values of the flux additional vortex periodicities arise, determined by the following relation between the atomic filling and vortex density $\rho_v = 1 - \rho$ [28, 40]. In Sec. V D we further discuss the presence of the commensurability effects present at large values of the interaction strength.

By increasing the interaction strength, from $U/J = 1$ in Fig. 2(a) to $U/J = 10$ in Fig. 2(b) we can see that the main changes occurring to the phase boundaries are due to the sensitivity on interactions of the biased chiral superfluid phase. For $U/J = 1$ the BC-SF extends to smaller values of the flux, $\chi < 0.5\pi$ and we can even trace it as a narrow intermediate phase between the M-SF and V-SF up to at least $J_{\parallel}/J \approx 1.3$. However, by increasing the interactions to $U/J = 10$ the BC-SF only occurs for $\chi \gtrsim 0.85\pi$ and we do not find a direct transition from the M-SF to the BC-SF, only via the V-SF.

In the following sections we present the behavior of the Hall response throughout the phase diagram, considering the interaction dependence from the weakly to the strongly interacting limits.

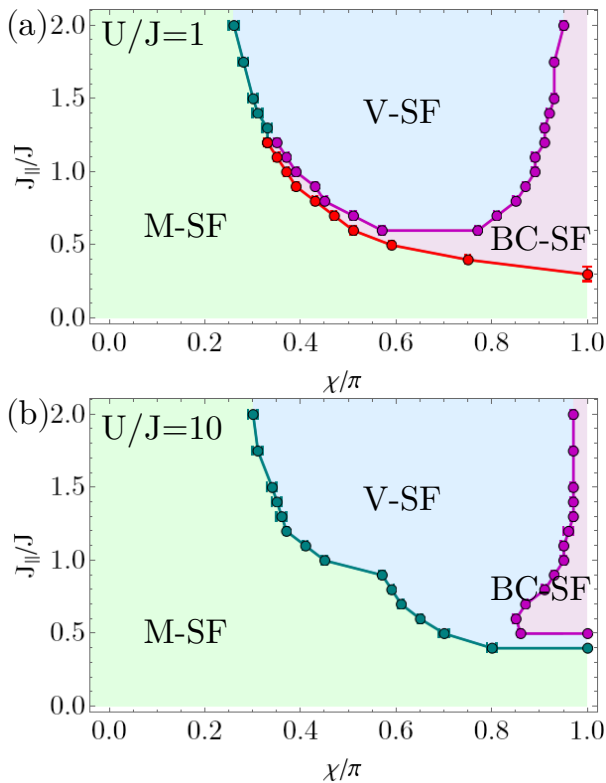


FIG. 2: Sketch of the phase diagram for $\rho = 0.25$ with (a) $U/J = 1$, (b) $U/J = 10$. The phases present for these parameters are the Meissner superfluid (M-SF), the vortex superfluid (V-SF) and biased chiral superfluid (BC-SF). The nature of the quantum phases was identified based on DMRG numerical simulations analyzed similarly as in Ref. [40] for a system size of $L = 120$ sites on each leg. The symbols depicted correspond to the values of the flux χ/π at which the phase transitions occur determined numerically for a fixed value of J_{\parallel}/J . The main characteristics of the phases are described in Sec. V.

A. The Hall response of the Meissner phase

We begin by analyzing the behavior of the Hall polarization in the Meissner superfluid phase. In Fig. 3 we show the dependence of the steady value of the Hall polarization $\langle\langle P_H \rangle\rangle$ as a function of the flux for small values of $J_{\parallel}/J < 0.2$ and different values of the interaction, from almost non-interacting atoms $U/J = 0.1$, to the hardcore limit $U/J = \infty$, within the Meissner superfluid phase. For $J_{\parallel}/J = 0.05$, Fig. 3(a), the dependence on the flux is almost symmetric with a maximum around the value $\chi/\pi = 0.5$. However, we can observe that by increasing J_{\parallel}/J the maximum of $\langle\langle P_H \rangle\rangle$ increases in magnitude and moves to higher values of χ . As will be discussed in Sec. VB, this is due to the proximity of the phase transitions to either to the vortex phase or to the biased chiral superfluid, effect which is more prominent at lower values of the interaction strength. At low values of the flux, $\chi/\pi \lesssim 0.15$, we have a very good agreement with the equilibrium value of the Hall polarization computed

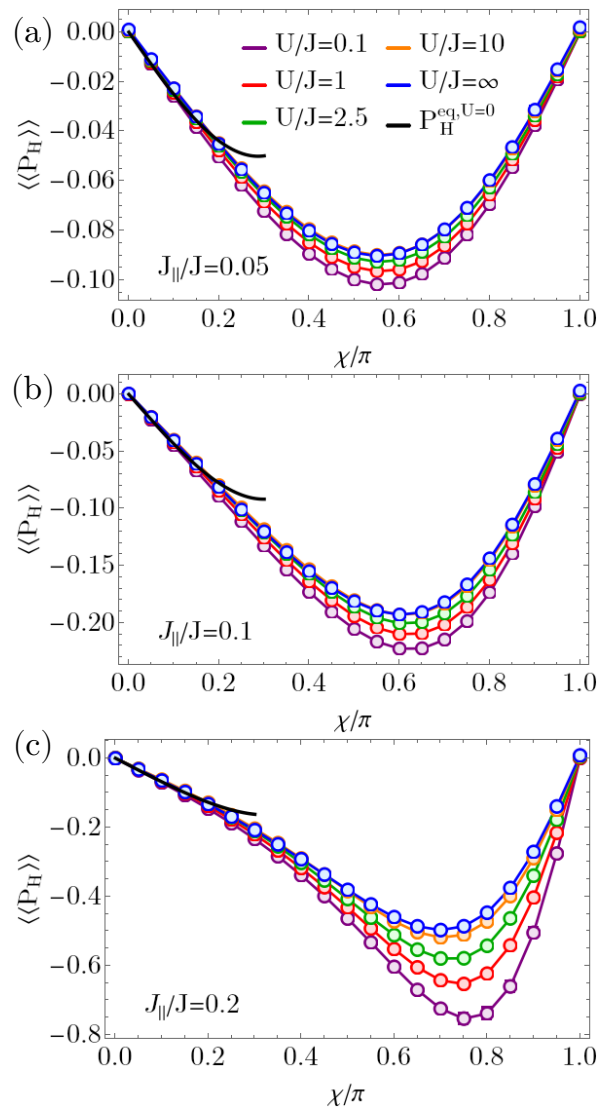


FIG. 3: Time-averaged Hall polarization $\langle\langle P_H \rangle\rangle$ in the Meissner superfluid phase as a function of χ for (a) $J_{\parallel}/J = 0.05$, (b) $J_{\parallel}/J = 0.1$, (c) $J_{\parallel}/J = 0.2$, for different values of the interaction strength U . The system size used is $L = 60$, filling $\rho = 0.25$ and the strength of the linear potential $\mu/J = 0.01$. The black curve at small values of the flux corresponds to the analytical value $P_H^{eq, U=0}$, Eq. (11).

for non-interacting bosons, $P_H^{eq, U=0}$. This is also due to the fact that the on-site interaction does not seem to play an important role in this regime, as seen in Fig. 4(a) for $J_{\parallel}/J = 0.2$ and $\chi/\pi = 0.1$, where in between $U/J = 2$ and the hardcore limit $\langle\langle P_H \rangle\rangle$ is mostly independent on the value of the interaction. However, for larger values of the magnetic flux, e.g. in Fig. 4(b) for $J_{\parallel}/J = 0.2$ and $\chi/\pi = 0.7$, the value of U/J is much more important, with the magnitude of $\langle\langle P_H \rangle\rangle$ decreasing with increasing the interaction strength.

The good agreement between the analytical expression of $P_H^{eq, U=0}$, Eq. (11), and the numerically determined $\langle\langle P_H \rangle\rangle$ for small values of the interaction, $U/J = 0.1$ and

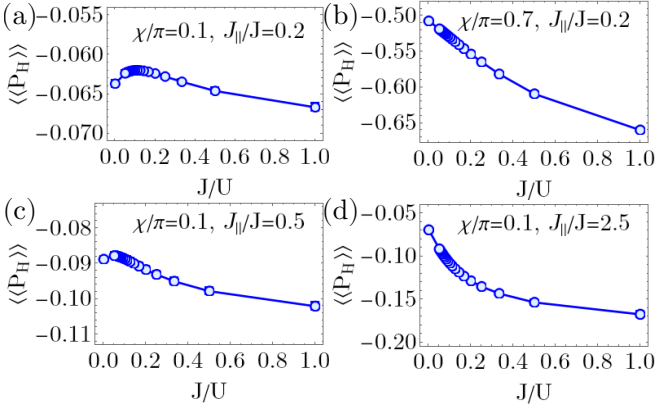


FIG. 4: Time-averaged Hall polarization $\langle\langle P_H \rangle\rangle$ in the Meissner superfluid phase as a function of J/U for (a) $\chi = 0.1\pi$, $J_{\parallel}/J = 0.2$, (b) $\chi = 0.7\pi$, $J_{\parallel}/J = 0.2$, (c) $\chi = 0.1\pi$, $J_{\parallel}/J = 0.5$, (d) $\chi = 0.1\pi$, $J_{\parallel}/J = 2.5$. The system size used is $L = 90$, filling $\rho = 0.25$ and the strength of the linear potential $\mu/J = 0.001$.

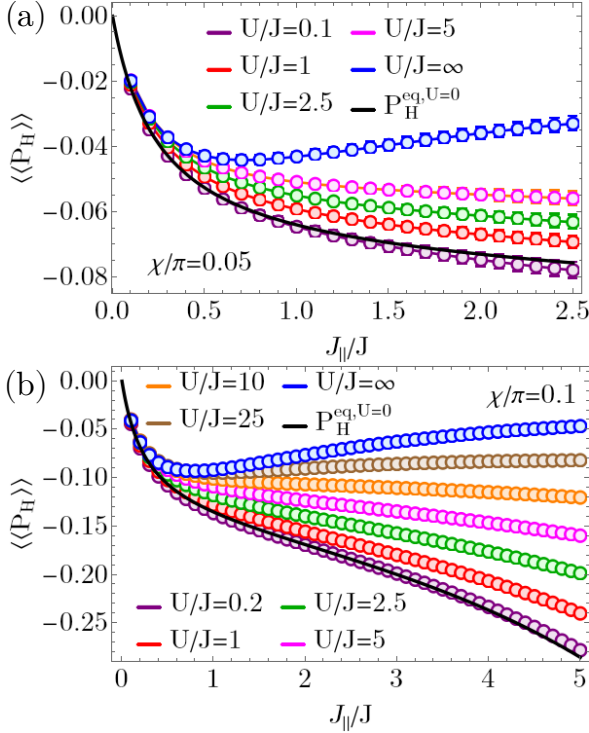


FIG. 5: Time-averaged Hall polarization $\langle\langle P_H \rangle\rangle$ in the Meissner superfluid phase as a function of J_{\parallel}/J for (a) $\chi = 0.05\pi$, (b) $\chi = 0.1\pi$, for different values of the interaction strength U . The system size used is (a) $L = 60$, (b) $L = 90$, filling $\rho = 0.25$ and the strength of the linear potential (a) $\mu/J = 0.01$, (b) $\mu/J = 0.001$. The black curve at small values of the flux corresponds to the analytical value $P_H^{\text{eq}, U=0}$, Eq. (11).

$U/J = 0.2$, can be very well seen in Fig. 5, where we depict $\langle\langle P_H \rangle\rangle$ as a function of J_{\parallel}/J for small values of χ . The weak dependence of the interaction is confined only to small J_{\parallel}/J , while for larger values we have a

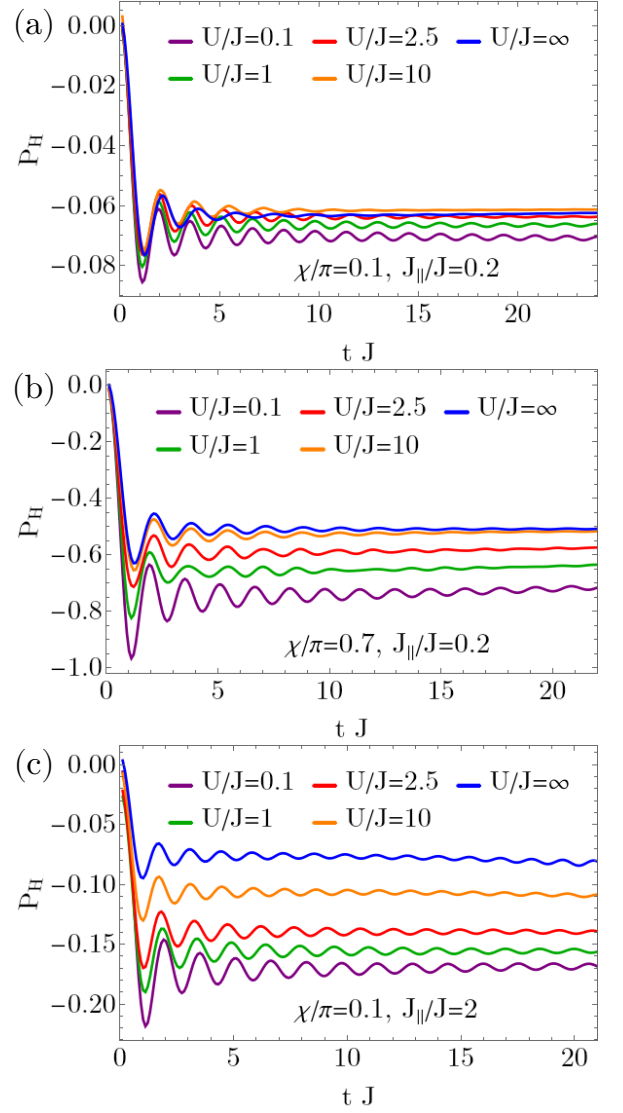


FIG. 6: Time evolution of the Hall polarization $P_H(t)$ in the Meissner superfluid phase for (a) $\chi = 0.1\pi$, $J_{\parallel}/J = 0.2$, (b) $\chi = 0.7\pi$, $J_{\parallel}/J = 0.2$, (c) $\chi = 0.1\pi$, $J_{\parallel}/J = 2$, for different values of the interaction strength U . The system size used is (a), (c) $L = 90$ and (b) $L = 60$, and the strength of the linear potential (a), (c) $\mu/J = 0.001$ and (b) $\mu/J = 0.01$.

much stronger influence of the interaction, for example see also Fig. 4(c) for $J_{\parallel}/J = 0.5$ in contrast to Fig. 4(d) for $J_{\parallel}/J = 2.5$. Furthermore, we observe in Fig. 5 that the value of U/J is crucial for the dependence of $\langle\langle P_H \rangle\rangle$ as a function on J_{\parallel}/J at larger values of J_{\parallel}/J . While for hardcore bosons the Hall polarization is decreasing with J_{\parallel}/J , for $U/J \lesssim 10$ $\langle\langle P_H \rangle\rangle$ is increasing with J_{\parallel}/J for the interval shown. We associate this with the fact that a phase transition to the vortex superfluid phase might occur for larger values of J_{\parallel}/J even for the values of χ shown in Fig. 5, e.g. for the non-interacting case the phase transition occurs for $J_{\parallel}/J \approx 10$ for $\chi/\pi = 0.1$, see Sec. VB for more details about the behavior approaching

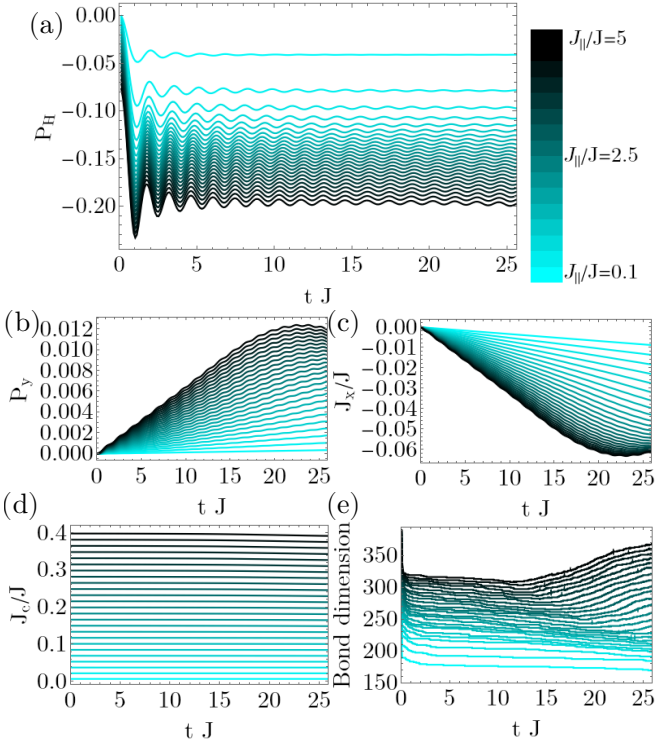


FIG. 7: Time evolution in the Meissner superfluid phase of the (a) Hall polarization P_H , (b) density imbalance P_y , (c) current \mathbf{J}_x/J , (d) chiral current J_c/J , and (e) bond dimension, for $\chi = 0.1\pi$, $U/J = 2.5$, for different values of the tunneling amplitude J_{\parallel}/J , in between $J_{\parallel}/J = 0.1$ and $J_{\parallel}/J = 5$. The system size used is $L = 90$, and the strength of the linear potential $\mu/J = 0.001$.

the phase transition.

We depict the dynamics of $P_H(t)$ in the Meissner superfluid phase in Fig. 6 for different values of the interaction strength and in Fig. 7(a) varying the strength of J_{\parallel}/J . Throughout the Meissner phase we observe a similar dynamical behavior, a fast increase of the magnitude of P_H followed by damped oscillations towards the transient steady value. This steady behavior at long times justifies the study of the time averaged Hall polarization $\langle\langle P_H \rangle\rangle$. In Fig. 6 we observe, for all parameters depicted, that the oscillations are more prominent for small value of the interaction strength, their damping increasing with the value of U/J , which also has a slight impact on the frequency of the oscillations.

In Fig. 7 we monitor the state of the system following the quench of the linear potential for $\chi = 0.1\pi$, $U/J = 2.5$ and a wide range of the tunneling $0.1 \leq J_{\parallel}/J \leq 5$, for times up to $tJ = 25$. We observe a well defined plateau in the Hall polarization [Fig. 7(a)] for times considered, with the value of $\langle\langle P_H \rangle\rangle$ increasing with J_{\parallel}/J for these parameters. Following the quench of the linear potential the magnitude of both the density imbalance $\langle P_y \rangle$ and the current $\langle \mathbf{J}_x \rangle$ exhibits a mostly linear increase. For larger values of J_{\parallel}/J , we can see a deviation from the

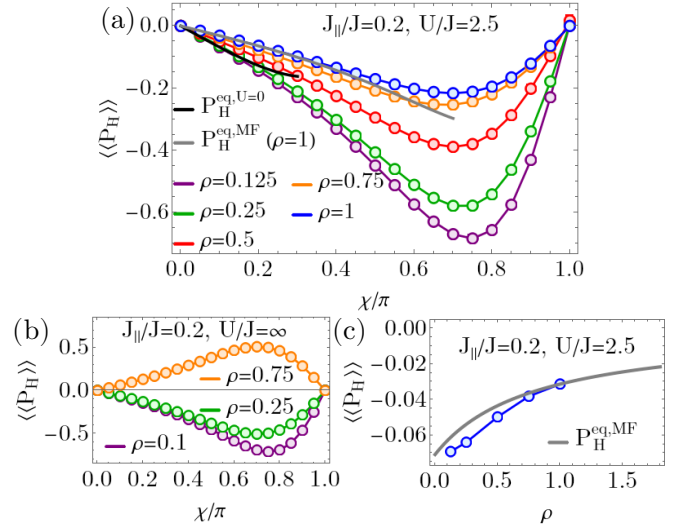


FIG. 8: Time-averaged Hall polarization $\langle\langle P_H \rangle\rangle$ in the Meissner superfluid phase as a function of χ for (a) $J_{\parallel}/J = 0.2$, $U/J = 2.5$, (b) $J_{\parallel}/J = 0.2$, $U/J = \infty$, for different values of the filling ρ , and (c) as a function of ρ for $J_{\parallel}/J = 0.2$, $U/J = 2.5$. The system size used is (a), (c) $L = 60$ and (b) $L = 90$, and the strength of the linear potential (a), (c) $\mu/J = 0.01$ and (b) $\mu/J = 0.001$. The black curve at small values of the flux corresponds to the analytical value $P_H^{\text{eq}, U=0}$, Eq. (11), and the gray curve corresponds to the analytical value $P_H^{\text{eq}, \text{MF}}(\rho = 1)$, Eq. (14). We note that in panel (b) the values shown for $\rho = 0.25$, $U/J = \infty$ are taken from Ref. [28].

linear trend for times $tJ \gtrsim 20$, stemming from the finite size of the ladder considered here. For larger system size, or smaller values of the linear potential μ/J , the deviation from the linear evolution would occur at later times. Interestingly, for the parameters and times considered we see that the plateau value of P_H is not affected.

In order to analyze the nature of the state during the evolution we compute the dynamics of the chiral current, defined as

$$J_c = \frac{1}{2(L-1)} \sum_j \langle j_{j,1}^{\parallel} - j_{j,2}^{\parallel} \rangle, \quad \text{with} \quad (15)$$

$$j_{j,m}^{\parallel} = -iJ_{\parallel} \left[e^{i\chi(-1)^m} b_{j,m}^{\dagger} b_{j+1,m} - \text{H.c.} \right].$$

We can see that $J_c(t)$ remains constant in time and equal to its ground state value, Fig. 7(d). This implies that the system maintains its Meissner superfluid character also after the quench during the time interval from which we extract its Hall response. Furthermore, in Fig. 7(e) we show the evolution of the bond dimension used to represent the state of the system as a MPS, which roughly quantifies the amount of entanglement present [48]. We observe that by keeping the truncation error fixed to 10^{-12} the bond dimension decreases abruptly at short times and remains almost constant during the time interval which exhibits a linear evolution of P_y and \mathbf{J}_x . We associate the increase at late times with the growing importance of the boundary effects, thus, offering us a

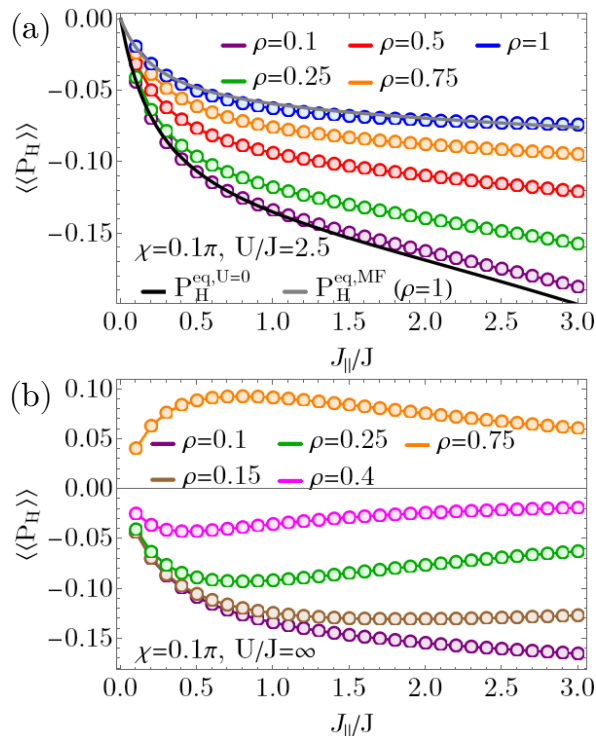


FIG. 9: Time-averaged Hall polarization $\langle\langle P_H \rangle\rangle$ in the Meissner superfluid phase as a function of J_{\parallel}/J for $\chi = 0.1\pi$ and (a) $U/J = 2.5$, (b) $U/J = \infty$, for different values of the filling ρ . The system size used is $L = 90$, and the strength of the linear potential $\mu/J = 0.001$. In (a), the black curve at small values of the flux corresponds to the analytical value $P_H^{\text{eq}, U=0}$, Eq. (11), and the gray curve corresponds to the analytical value $P_H^{\text{eq}, \text{MF}}(\rho = 1)$, Eq. (14).

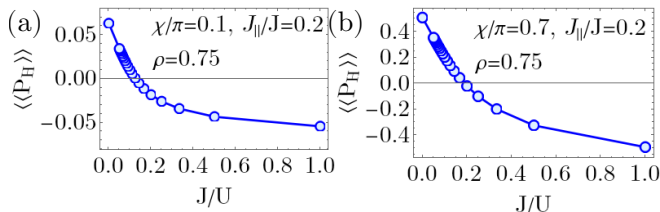


FIG. 10: Time-averaged Hall polarization $\langle\langle P_H \rangle\rangle$ in the Meissner superfluid phase as a function of J/U for (a) $\chi = 0.1\pi$, $J_{\parallel}/J = 0.2$, (b) $\chi = 0.7\pi$, $J_{\parallel}/J = 0.2$. The system size used is $L = 90$, filling $\rho = 0.75$ and the strength of the linear potential $\mu/J = 0.001$.

further handle to the estimation of the influence of finite size.

In the final part of the section regarding the Hall response in the Meissner superfluid phase, we analyze the role of the atomic filling ρ with the results presented in Fig. 8 and Fig. 9. For a finite interaction strength of $U/J = 2.5$ increasing the atomic filling decreases the magnitude of the Hall polarization, as seen in Fig. 8(a) as a function of χ for $J_{\parallel}/J = 0.2$ and in Fig. 9(a) as a function of J_{\parallel}/J for $\chi = 0.1\pi$. In the case of small values

of ρ we compare our numerical results with the analytical result $P_H^{\text{eq}, U=0}$, Eq. (11), [black curves in Fig. 8(a) and Fig. 9(a)], as the non-interacting Hall polarization also corresponds to the single particle limit. We obtain a good agreement with $\langle\langle P_H \rangle\rangle$ for $\rho = 0.125$ for a magnetic flux up to $\chi \lesssim 0.15\pi$ [Fig. 8(a)] and for $\rho = 0.1$ and $\chi = 0.1\pi$ for the dependence on J_{\parallel}/J [Fig. 9(a)]. The second comparison we perform is for larger values of the atomic filling, where we expect the mean-field approach presented in Sec. IV B to hold. For $\rho = 1$, $P_H^{\text{eq}, \text{MF}}(\rho = 1)$, Eq. (14), agrees well with the numerical results for $\chi \lesssim 0.4\pi$ and the dependence on J_{\parallel}/J , see gray curves in Fig. 8(a) and Fig. 9(a). Furthermore, in Fig. 8(c) we can see that the agreement with the mean-field result becomes better as we increase ρ .

As for hardcore bosons a particle-hole symmetry is present in the system for $\rho = 0.5$, it is interesting to investigate the dependence on the filling also in this case. We expect that from small fillings the magnitude of the Hall response will decrease with ρ until it vanishes for $\rho = 0.5$ and changes signs for larger fillings, with the same magnitude and opposite signs for ρ and $1 - \rho$. We observe this behavior in Fig. 8(b) and Fig. 9(b), in particular we obtain the same value $|\langle\langle P_H \rangle\rangle|$ for $\rho = 0.25$ and $\rho = 0.75$, but $\langle\langle P_H \rangle\rangle$ has opposite sign for the two values of the filling. The change in sign of the Hall polarization offers us an interesting opportunity when $\rho > 0.5$, as in weak interactions $\langle\langle P_H \rangle\rangle$ is negative in the Meissner phase, while for hardcore bosons $\langle\langle P_H \rangle\rangle$ is positive. This implies that by varying the on-site interaction strength from weakly to strongly interacting regimes we can change the sign of the Hall polarization and have a value of U/J for which the Hall response vanishes. For example, we depict this behavior in Fig. 10 for $\rho = 0.75$ for two sets of parameters in the Meissner superfluid phase. It is an interesting open question if a symmetry emerges at the particular value of U/J for which the Hall response vanishes.

B. Hall response across phase transitions

In the following section we analyze the behavior of the Hall polarization as we vary the parameters of the model to cross from the Meissner superfluid to the biased-chiral superfluid and the vortex superfluid. In Fig. 11 we show $\langle\langle P_H \rangle\rangle$ as a function of J_{\parallel}/J for $\chi \in \{0.3\pi, 0.5\pi, 0.8\pi, 0.9\pi\}$ for several values of the interaction, for which the system crosses at least one phase boundary. We can observe a very rich behavior, with large values of the Hall response, either negative, or positive, implying the change of sign of the Hall polarization, and a strong dependence on the value of U/J .

We focus first on the divergence-like feature we observe as we approach the phase transition to the vortex or biased phases from the Meissner phase, as we increase J_{\parallel}/J , e.g. around $J_{\parallel}/J \approx 0.7 - 1.5$ in Fig. 11(a), or around $J_{\parallel}/J \approx 0.2 - 1.4$ in Fig. 11(c). We can understand this behavior already in the non-interacting limit,

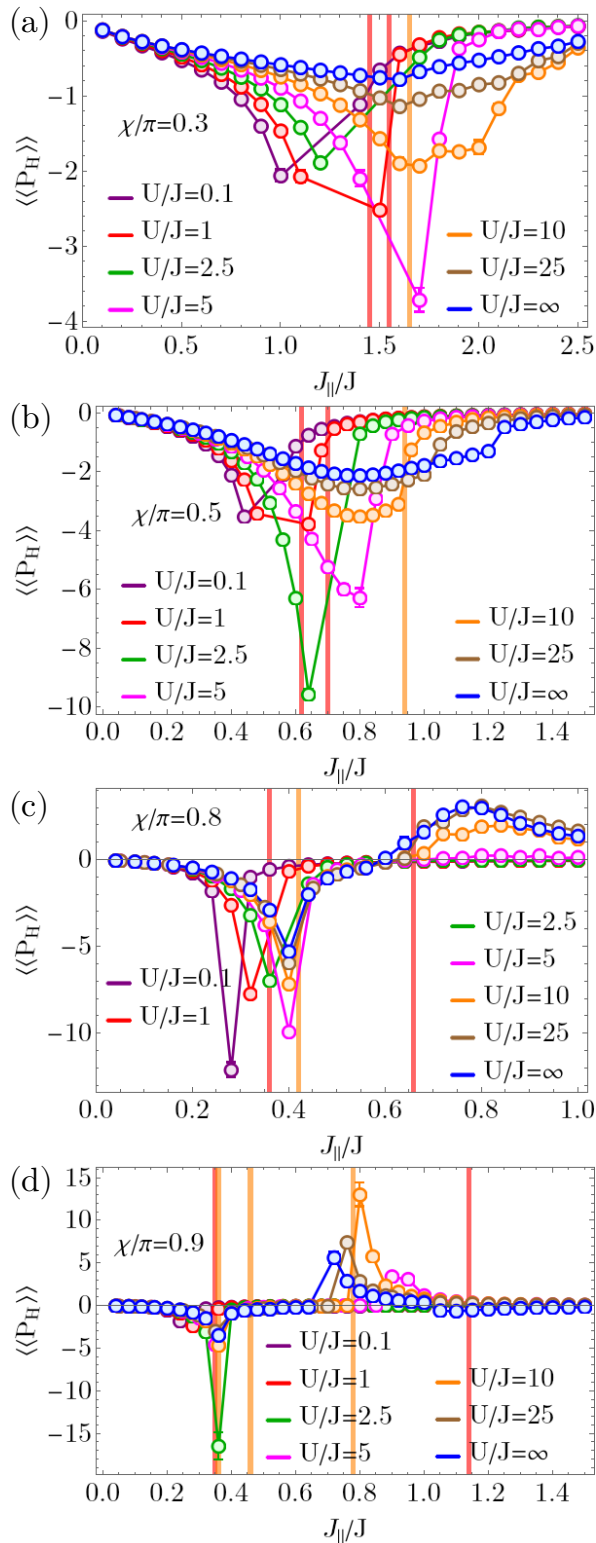


FIG. 11: Time-averaged Hall polarization $\langle\langle P_H \rangle\rangle$ across phase transitions as a function of J_{\parallel}/J for (a) $\chi = 0.3\pi$, (b) $\chi = 0.5\pi$, (c) $\chi = 0.8\pi$, (d) $\chi = 0.9\pi$, for different values of the interaction strength U . The system size used is $L = 90$, filling $\rho = 0.25$ and the strength of the linear potential $\mu/J = 0.001$. The vertical lines denote the phase transition threshold values for $U/J = 1$ in red and $U/J = 10$ in orange as marked in the ground state phase diagrams in Fig. 2.

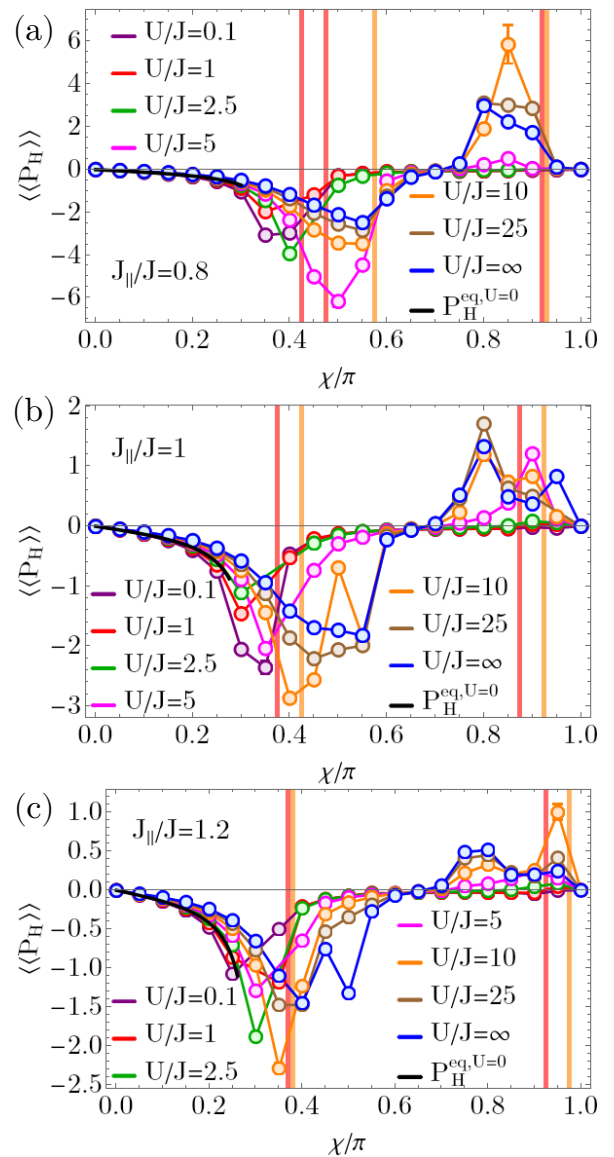


FIG. 12: Time-averaged Hall polarization $\langle\langle P_H \rangle\rangle$ as a function of χ for (a) $J_{\parallel}/J = 0.8$, (b) $J_{\parallel}/J = 1$, (c) $J_{\parallel}/J = 1.2$, for different values of the interaction strength U . The system size used is $L = 90$, filling $\rho = 0.25$ and the strength of the linear potential $\mu/J = 0.001$. The black curve at small values of the flux corresponds to the analytical value $P_H^{\text{eq}, U=0}$, Eq. (11). The vertical lines denote the phase transition threshold values for $U/J = 1$ in red and $U/J = 10$ in orange as marked in the ground state phase diagrams in Fig. 2. We note that in panel (a) the values shown for hardcore bosons, $U/J = \infty$, are taken from Ref. [28].

as in the following. For $U/J = 0$, the dispersion relation of the Hamiltonian is given by the expression in Eq. (10) for $\tilde{\Phi} = 0$, the lower band exhibits either a single, or a double minimum structure depending on the chosen parameters [40]. The Meissner phase is characterized by a single minimum, while the vortex and biased-chiral phase by two minima, with the transition thresh-

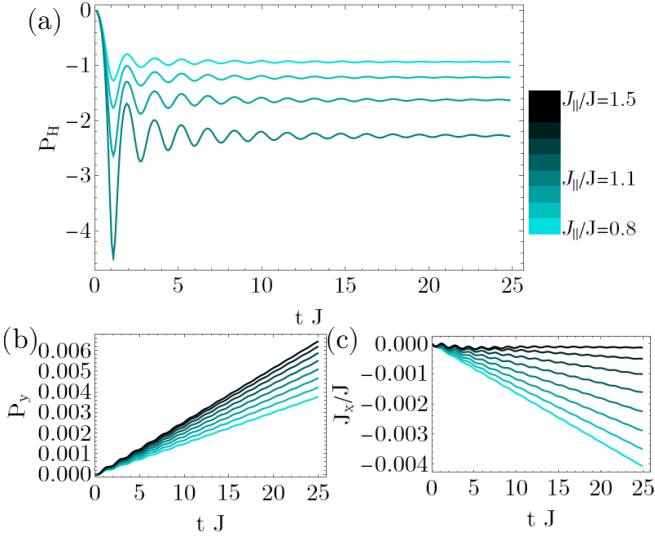


FIG. 13: Time evolution in the Meissner superfluid phase towards the phase transition threshold of the (a) Hall polarization P_H , (b) density imbalance P_y , (c) current \mathbf{J}_x/J , for $\chi = 0.3\pi$, $U/J = 1$, for different values of the tunneling amplitude J_{\parallel}/J , in between $J_{\parallel}/J = 0.8$ and $J_{\parallel}/J = 1.1$ for P_H and up to $J_{\parallel}/J = 1.5$ for P_y and \mathbf{J}_x/J . The system size used is $L = 90$, and the strength of the linear potential $\mu/J = 0.001$.

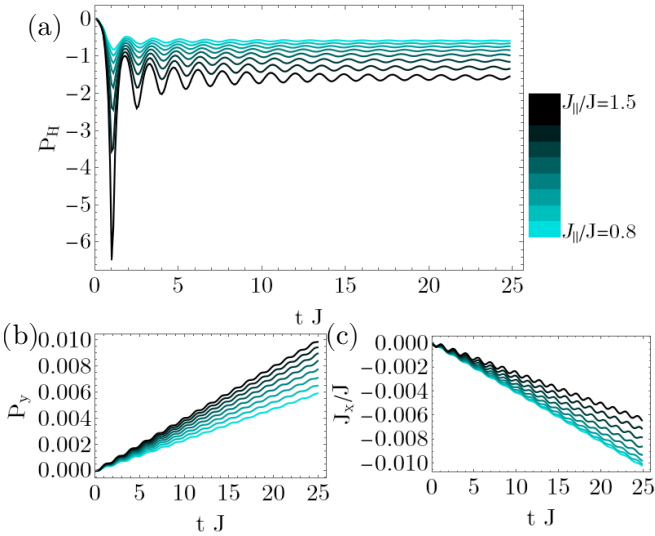


FIG. 14: Time evolution in the Meissner superfluid phase towards the phase transition threshold of the (a) Hall polarization P_H , (b) density imbalance P_y , (c) current \mathbf{J}_x/J , for $\chi = 0.3\pi$, $U/J = 10$, for different values of the tunneling amplitude J_{\parallel}/J , in between $J_{\parallel}/J = 0.8$ and $J_{\parallel}/J = 1.5$. The system size used is $L = 90$, and the strength of the linear potential $\mu/J = 0.001$.

old being defined by the parameters for which the lower band has a quartic minimum and satisfy the condition $1 + 4(J_{\parallel}/J) \cos(\chi) - 4(J_{\parallel}/J)^2 \sin(\chi)^2 = 0$. However, for the parameters satisfying this condition also the current $\langle \mathbf{J}_x \rangle^{\text{eq}}$ vanishes, which implies that $P_H^{\text{eq}, U=0}$ diverges

as we approach the phase boundary from the Meissner phase, due to the change in the structure of the dispersion relation. In Fig. 12 we can see the good agreement as we approach the divergence of $P_H^{\text{eq}, U=0}$ (black curves) as a function of χ , with the numerical result for weak interactions of $U/J = 0.1$ (purple points).

In the numerical results at finite interaction strengths we do not expect that the current will vanish at the phase transition to obtain a divergence. However, for our protocol in which we quench a linear potential, presented in Sec. II, even if the arising current is non-zero it can have values comparable with the amplitude of the oscillations present a short times. Thus, for weak interactions close to the phase boundary between M-SF and V-SF, or BC-SF, the short-time oscillations of current can determine a zero value of the current at certain points in time, which can prevent a well defined Hall polarization, Eq. (4). For example, in Fig. 13(a) for $U/J = 1$, we have a nicely behaved $P_H(t)$ for $0.8 \leq J_{\parallel}/J \leq 1.1$, but for larger values of the tunneling $1.2 \leq J_{\parallel}/J \leq 1.5$, the current crosses zero at several points in time, as seen in Fig. 13(c). This is the reason why in Fig. 11 for small values of the interactions, $U/J \lesssim 2$, we have points missing for certain values of the tunneling amplitude J_{\parallel}/J for which we could not properly define a time-averaged $\langle\langle P_H \rangle\rangle$. Roughly for values larger than $U/J = 2.5$ we do not see the current crossing zero in its time-evolution for the parameters consider. For $U/J = 10$, results shown in Fig. 14, we observe oscillations in both the current and the density imbalance [Fig. 14(b),(c)], but as the magnitude of the current is large enough, such that we can extract a meaningful Hall polarization up to the phase boundary. Even if for strong on-site interactions we do not have a divergence of the Hall polarization, we still see an influence of this single particle effect. As observe in Fig. 11(a),(c),(d), by approaching the phase boundary marking the end of the Meissner phase $\langle\langle P_H \rangle\rangle$ increases rapidly with its maximum close to the critical point and, in most cases, followed by an abrupt decrease in its magnitude in the subsequent phase. Interestingly, in Fig. 11(b), where the flux is $\chi = 0.5\pi$, for $U/J \geq 10$ we observe that the maximum of $\langle\langle P_H \rangle\rangle$ as a function of J_{\parallel}/J does not correspond to the phase transition threshold, but rather is in the Meissner phase. However, also for these parameters after the phase transition we see a discontinuous jump in the value of $\langle\langle P_H \rangle\rangle$.

C. The Hall response of the biased-chiral superfluid phase

In this section we investigate the behavior of the Hall polarization in the biased-chiral superfluid, phase characteristic to the triangular ladder having its origin in the frustrated nature of the system at larger values of the flux [40]. We focus on the parameter regime for which the BC-SF phase has a larger extent, e.g. for $\chi = 0.8\pi$ in Fig. 11(c) for $U/J = 1$ we are in the BC-SF for

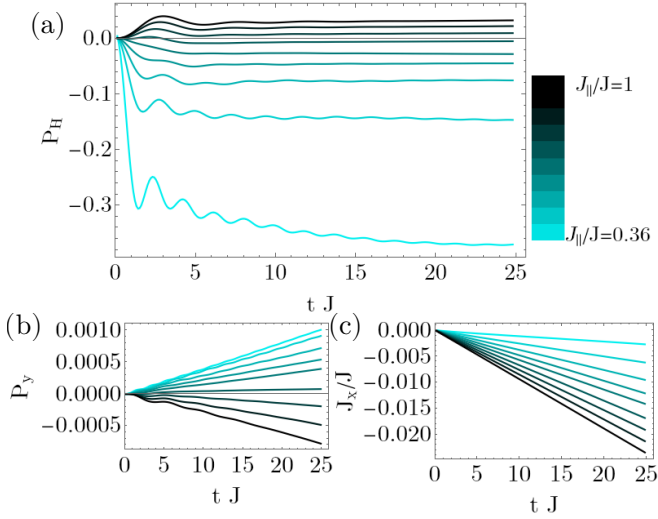


FIG. 15: Time evolution in the biased-chiral superfluid phase of the (a) Hall polarization P_H , (b) density imbalance P_y , (c) current \mathbf{J}_x/J , for $\chi = 0.9\pi$, $U/J = 1$, for different values of the tunneling amplitude J_{\parallel}/J , in between $J_{\parallel}/J = 0.36$ and $J_{\parallel}/J = 1$. The system size used is $L = 90$, and the strength of the linear potential $\mu/J = 0.001$.

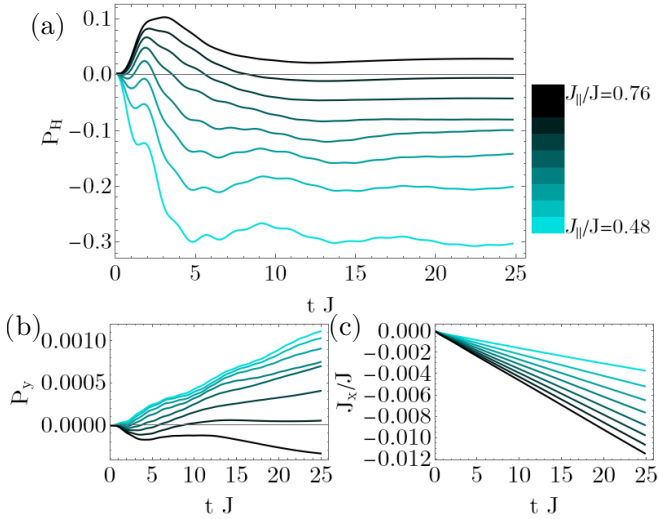


FIG. 16: Time evolution in the biased-chiral superfluid phase of the (a) Hall polarization P_H , (b) density imbalance P_y , (c) current \mathbf{J}_x/J , for $\chi = 0.9\pi$, $U/J = 10$, for different values of the tunneling amplitude J_{\parallel}/J , in between $J_{\parallel}/J = 0.48$ and $J_{\parallel}/J = 0.76$. The system size used is $L = 90$, and the strength of the linear potential $\mu/J = 0.001$.

$0.36 \lesssim J_{\parallel}/J \lesssim 0.66$, or for $\chi = 0.9\pi$ in Fig. 11(d) for $U/J = 1$ we are in the BC-SF for $0.35 \lesssim J_{\parallel}/J \lesssim 1.14$ and for $U/J = 10$ we are in the BC-SF for $0.46 \lesssim J_{\parallel}/J \lesssim 0.78$ (see also the phase diagrams in Fig. 2). $\langle\langle P_H \rangle\rangle$ in these regimes has a smooth behavior and relatively small values, in contrast to the behavior close to the transition thresholds, or in the vortex phase (see Sec. VD). However, we observe a change of sign of the Hall polarization

as we increase the tunneling amplitude J_{\parallel}/J . For this change of sign we lack an explanation similar to the one in Sec. VA based on the change of the nature of carriers in the hardcore regime. Furthermore, we obtain the same value of the Hall polarization for both symmetry broken states that span the ground state manifold of the BC-SF, regardless of their sign of the ground state density imbalance.

The dynamics of P_H in the BC-SF is shown in Fig. 15 for $U/J = 1$ and in Fig. 16 for $U/J = 10$, together with the time-dependence of the density imbalance P_y and current \mathbf{J}_x/J . We observe that for both weak and strong interactions the dynamical behavior in the biased phase is different compared to what we saw in the previous section for the Meissner phase, giving a further motivation to investigate also the dynamics of the Hall polarization and not only its steady value. In the case of $U/J = 1$, Fig. 15(a), close to the phase boundary for $J_{\parallel}/J = 0.36$ the Hall polarization reaches a steady value only for times $tJ \gtrsim 20$, while for larger values J_{\parallel}/J , deeper in the BC-SF, we reach faster the transient steady value, close to the parameters for which $\langle\langle P_H \rangle\rangle$ changes sign the fast initial oscillations are replaced with a slower oscillatory behavior. The main features of the dynamics, and the change of sign, are due to the time-dependence of the density imbalance P_y , as seen in Fig. 15(b), while the current has a mostly linear time evolution, Fig. 15(c). Similarly, also for stronger interactions, $U/J = 10$ shown in Fig. 16, it seems that the oscillatory features of $P_H(t)$ stem from the dynamics of P_y . In this regime, we observe that the sign of P_H is not necessarily determined at short times, as we can have an initial increase to positive values after which a relaxation to either positive, $J_{\parallel}/J = 0.76$, or negative, $J_{\parallel}/J \lesssim 0.72$, values occurs, see Fig. 16(a).

D. Emergence of commensurability effects at large interaction

In this section, we analyze the Hall polarization in the vortex superfluid phase, with a particular focus on the commensurability effects which are the cause of the strong positive response observed in Fig. 11 and Fig. 12. We focus on understanding on how the strong positive Hall response emerges as we increase the strength of the interactions. For example, in Fig. 12(a) for $J_{\parallel}/J = 1$, we observe that for weak interactions in the vortex superfluid phase ($0.37\pi \lesssim \chi \lesssim 0.87\pi$ for $U/J = 1$) the stationary value of the Hall polarization has a smooth behavior with a rather small magnitudes as a function of the flux. In the case of $U/J = 1$ the values remain of $\langle\langle P_H \rangle\rangle$ remain negative, by increasing the interactions to $U/J = 2.5$ the magnitude of $\langle\langle P_H \rangle\rangle$ is still relatively small, but it exhibits a change of sign. Increasing the interactions to even larger values we observe a large positive response developing, with a peak around $\chi \approx 0.8\pi$ for $U/J \gtrsim 10$. We can also see this behavior in the time-dependence of the Hall polarization, by contrasting the

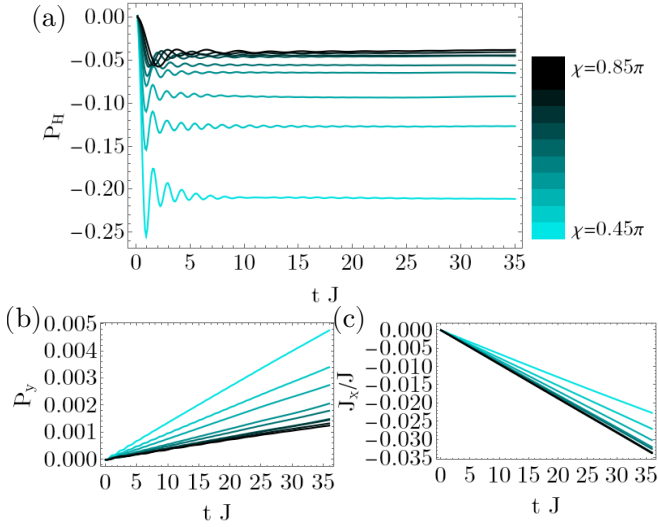


FIG. 17: Time evolution in the vortex superfluid phase of the (a) Hall polarization P_H , (b) density imbalance P_y , (c) current \mathbf{J}_x/J , for $J_{\parallel}/J = 1$, $U/J = 1$, for different values of the flux χ , in between $\chi = 0.45\pi$ and $\chi = 0.85\pi$. The system size used is $L = 90$, and the strength of the linear potential $\mu/J = 0.001$.

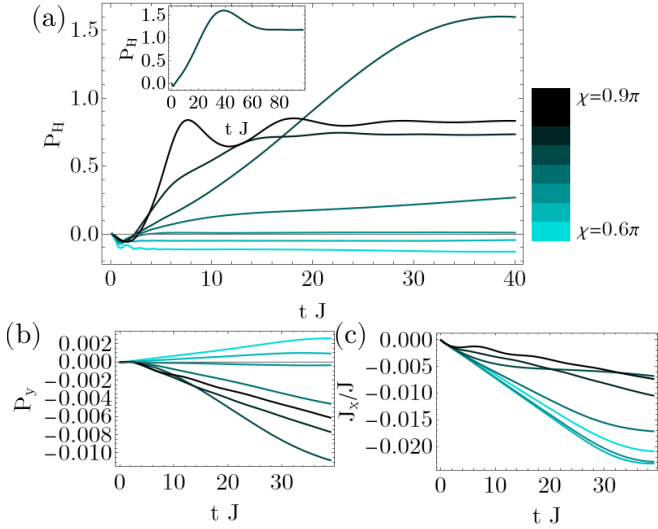


FIG. 18: Time evolution in the vortex superfluid phase of the (a) Hall polarization P_H , (b) density imbalance P_y , (c) current \mathbf{J}_x/J , for $J_{\parallel}/J = 1$, $U/J = 10$, for different values of the flux χ , in between $\chi = 0.6\pi$ and $\chi = 0.9\pi$. The inset in panel (a) contains the dynamics of P_H for $\chi = 0.8\pi$ up to longer times. The system size used is $L = 90$, and the strength of the linear potential $\mu/J = 0.001$.

results for $U/J = 1$ shown in Fig. 17, with the ones for $U/J = 01$ shown in Fig. 18. In Fig. 17(a) the dynamics of P_H the dynamics resembles the one in the Meissner phase, e.g. Fig. 7(a), with oscillations at short times that are damped to a steady values, even though for $\chi \gtrsim 0.7\pi$, as we approach the transition to the BC-SF, the period of the oscillations is larger and they persist to longer

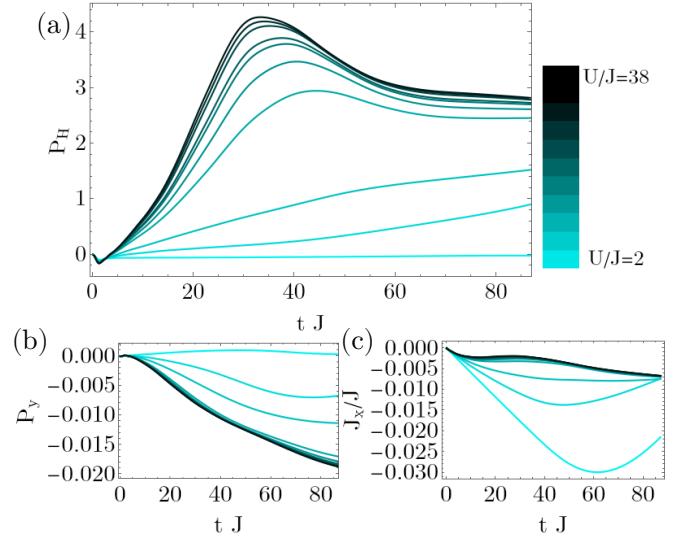


FIG. 19: Time evolution in the vortex superfluid phase of the (a) Hall polarization P_H , (b) density imbalance P_y , (c) current \mathbf{J}_x/J , for $J_{\parallel}/J = 0.76$, $\chi = 0.8\pi$, for different values of the interaction strength U , in between $U/J = 2$ and $U/J = 38$. The system size used is $L = 90$, and the strength of the linear potential $\mu/J = 0.001$.

times. This dynamical behavior is in contrast to what we observe in Fig. 18(a) for large values of the on-site interactions. Here after the sign change of the late time value around $\chi \approx 0.7\pi$, the dynamics is quite different, at very short times P_H is negative, but afterwards P_H starts increasing and becomes positive, due to a sign change of the polarization P_y for these values of the flux, Fig. 18(b). At even longer times we see a much slower dynamics towards a steady value than compared to the other phases investigated so far, in particular, for the largest value of $\langle\langle P_H \rangle\rangle$ occurring at $\chi = 0.8\pi$ a stationary behavior can be identified only for times larger than $tJ \gtrsim 60$ [see inset of Fig. 18(a)].

In Ref. [28] we have identified a similar behavior of saturation to large positive values after a slow dynamics in the case of hardcore bosons, which we attributed to the presence of a vortex density commensurate fixed by the value of the atomic filling. We found that the peak of the positive response strongly correlates with the parameters for which the commensurate vortex density dominates the expected incommensurate value of V-SF, for a wide range of parameters and atomic fillings. As this is similar to what we observe at strong finite interaction values, i.e. the strong positive Hall response appears as we increase the on-site interactions at the same time as the commensurate vortex density, we briefly sketch the origin of the second vortex density value [28]. One approach to deal with the Hamiltonian given in Eq. (1) for the case of hardcore, $U \rightarrow \infty$, interactions is to employ a Jordan-Wigner transformation to fermionic operators $c_j, b_j = \prod_{l=1}^{j-1} e^{i\pi c_l^\dagger c_l} c_j$. For a chain geometry, without other interactions, this transformation maps the hardcore

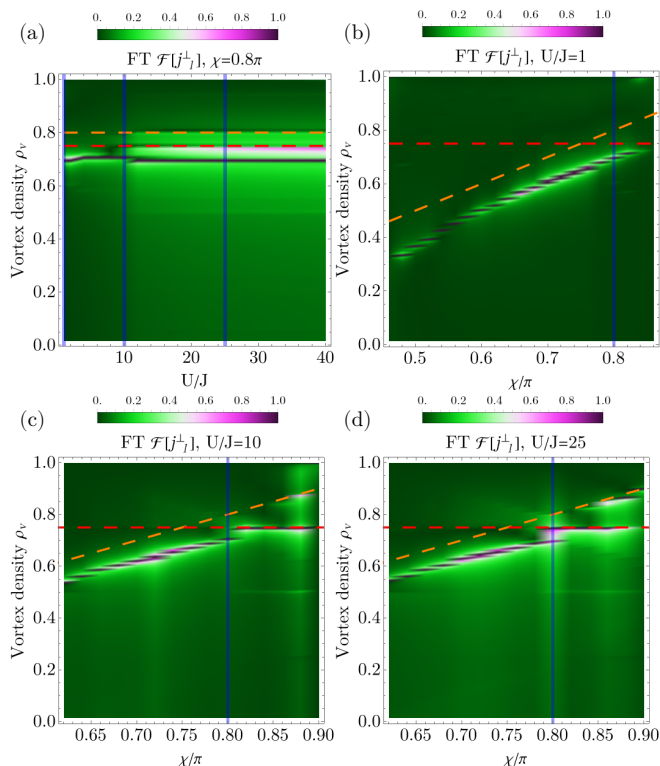


FIG. 20: The Fourier transform of the ground state local rung currents, j_j^\pm , as a function of (a) the on-site interactions U/J , (b)-(d) the flux χ for $J_\parallel/J = 0.76$, $\rho = 0.25$ and (a) $\chi = 0.8\pi$, (b) $U/J = 1$, (c) $U/J = 10$, (d) $U/J = 25$. The vertical axis has been scaled in terms of the vortex density ρ_v . The orange dashed lines corresponds to the expectation of the vortex superfluid phase of $\rho_v = \chi/\pi$, the red dashed lines corresponds to the value $\rho_v = 1 - \rho = 0.75$. In the vertical blue lines marks in (a) the interactions strengths used in panels (b)-(d), and in (b)-(d) the values of the flux used in panel (a). The system size used is (a) $L = 90$, (b)-(d) $L = 120$. We normalize the Fourier transform such that its maximum is equal to one for each column.

bosons to free fermions. In contrast, for our triangular geometry we obtain an interacting fermionic model as the Jordan-Wigner string does not cancel and we have in the Hamiltonian a term with four fermionic operators. In Ref. [28] we showed that by varying this term we interpolate between a free fermions equivalent of Eq. (1) and the hardcore bosons model, and for intermediate values of the fermionic interaction we obtain a vortex lattice superfluid with the vortex density $\rho_v = 1 - \rho$ determined by the atomic filling. Interestingly, even if we have a phase transition to the incommensurate vortex superfluid as we approach the hardcore bosons model we can still identify a peak corresponding to $\rho_v = 1 - \rho$ in the Fourier transform of the rung currents, which appears to determine a large positive value of the Hall polarization.

In Fig. 19(a) we show the time dependence of P_H for a wide range of the interactions $2 \leq U/J \leq 38$ up to long times, $tJ \gtrsim 80$, for parameters for which in the strongly

interacting limit we observe a strong positive response, for $J_\parallel/J = 0.76$ and $\chi = 0.8\pi$. For $U/J = 2$ we obtain a small negative stationary value, however we can only follow the dynamics up to times $tJ \approx 50$ before the finite size effects become important, as seen in the change of the monotony of the current in Fig. 19(c). Similarly, for the next two interaction strength values, $U/J = 6$ and $U/J = 10$, the finite size effects are relevant before we can identify a stationary Hall polarization. However, at even larger values $U/J > 10$ we can reliably compute the Hall polarization up to long times of $tJ \approx 80$ and identify at plateau for $tJ \gtrsim 60$ to which P_H stabilizes after a slow increase and an intermediate maximum. Next, we correlate the behavior of the Hall polarization with the ground state vortex density. We define the vortex density of the V-SF as the values for which we have a well defined peak in the Fourier transform of the ground state local rung currents, as shown in Fig. 21. In Fig. 21(a) we show the Fourier transform of the rung currents as a function of U/J , we see that for weak interaction we have a single vortex density $\rho_v \approx 0.7$, while around $U/J \approx 10$ multiple peaks appear in the Fourier transform, leading to the identification of multiple vortex densities. This corresponds exactly to the parameter regime of the large positive values of the Hall polarization. In order to understand better the vortex densities values present in the Fourier transform we plot the dependence on the flux for different U/J in Fig. 21(b)-(d). For $U/J = 1$, Fig. 21(b), we have a single vortex density varying linearly with the flux, corresponding to the expected incommensurate value of the vortex superfluid. We note the relation $\rho_v = \chi/\pi$ is only valid for large values of J_\parallel/J [40], but in Fig. 21 we consider $J_\parallel/J = 0.76$, explaining why even if ρ_v has a linear dependence, it does not exactly agree with the value χ/π . If we increase the interactions to $U/J = 10$ and $U/J = 25$ in Fig. 21(c)-(d), we observe an additional peak in the Fourier transform from which we can identify a vortex density $\rho_v = 0.75 = 1 - \rho$, for which the value is related to the atomic filling [28]. In particular, we can see that this commensurate vortex density dominates around $0.8\pi \lesssim \chi \lesssim 0.85\pi$, but without changing the two-mode gapless nature of the vortex phase [40]. For these values the incommensurate vortex density show a behavior similar to an avoided crossing, which explains why in Fig. 21(a) we see three peaks in the Fourier transform at $\chi = 0.8\pi$. We observe the same phenomenology also for the other parameters for which we see a large positive value of $\langle\langle P_H \rangle\rangle$ [see Fig. 11(c)-(d) and Fig. 12(a)-(c)], with a similar correspondence to the appearance of a dominant peak in the Fourier transform of the rung currents at $\rho_v = 1 - \rho$.

In the last part of this section we discuss the behavior of the Hall polarization for $\chi = 0.3\pi$ as we enter in the vortex superfluid phase, shown in Fig. 11(a). Compared to our previous discussion (see Sec. VB), we see an unusual behavior for $U/J = 10$ where $\langle\langle P_H \rangle\rangle$ does not exhibit a drop on its magnitude after crossing the phase boundary at $J_\parallel/J \approx 1.65$, as observed for the other

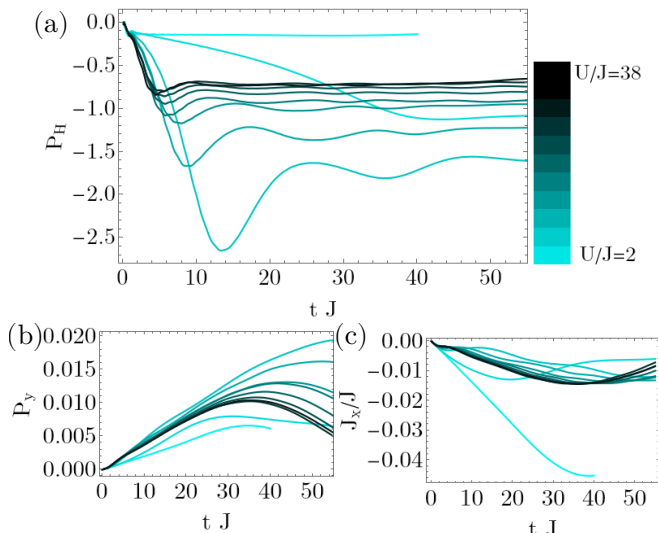


FIG. 21: Time evolution in the vortex superfluid phase of the (a) Hall polarization P_H , (b) density imbalance P_y , (c) current \mathbf{J}_x/J , for $J_{\parallel}/J = 2$, $\chi = 0.3\pi$, for different values of the interaction strength U , in between $U/J = 2$ and $U/J = 38$. The system size used is $L = 90$, and the strength of the linear potential $\mu/J = 0.001$.

parameters. One explanation for this could be that for $U/J = 10$ and $\chi = 0.3\pi$ by plotting $\langle\langle P_H \rangle\rangle$ as a function of J_{\parallel}/J we are really close the phase boundary for $J_{\parallel}/J \gtrsim 1.65$ [see Fig. 2(b)], while for the other interaction values the transition threshold is a slightly lower values of the flux. However, it is still interesting to analyze the time dependence of P_H , Fig. 21, and the behavior of the ground state vortex density, Fig. 22, for these parameters to gain additional insight. We can observe in Fig. 21(a) that increasing the interaction strength from $U/J = 2$ to $U/J = 6$ results in a drastic increase in the time scale for reaching the stationary value. For even stronger interactions, $U/J \geq 10$, the steady plateau is reached earlier, with the minimal value of $\langle\langle P_H \rangle\rangle$ reached for $U/J = 10$. The dynamics in this regime resembles the one showed in Fig. 18(a) for $\chi = 0.9\pi$, but with an opposite sign. By analyzing the behavior of the vortex density, we obtain that $U/J = 10$ is also the value for which multiple peaks in the Fourier transform of the rung currents appear, Fig. 22(a). For weak interactions [$U/J = 1$ in Fig. 22(b)], the vortex density is dominated by the incommensurate response $\rho_v = \chi/\pi$, with small deviations for smaller values of the flux close to the transition point to the Meissner phase. However, starting from $U/J = 10$ two additional peaks are present in the Fourier transform, corresponding to the vortex densities $\rho_v = 1 - \rho$ and $\rho_v = \rho$, which seem to lead to a strong Hall response. We note that we did not check for multiple parameter sets that the commensurate vortex density of $\rho_v = \rho$ within the vortex superfluid leads to a large negative value of $\langle\langle P_H \rangle\rangle$, as for the parameters considered in this work the vortex phase did not extent to low enough values of the flux. This is in

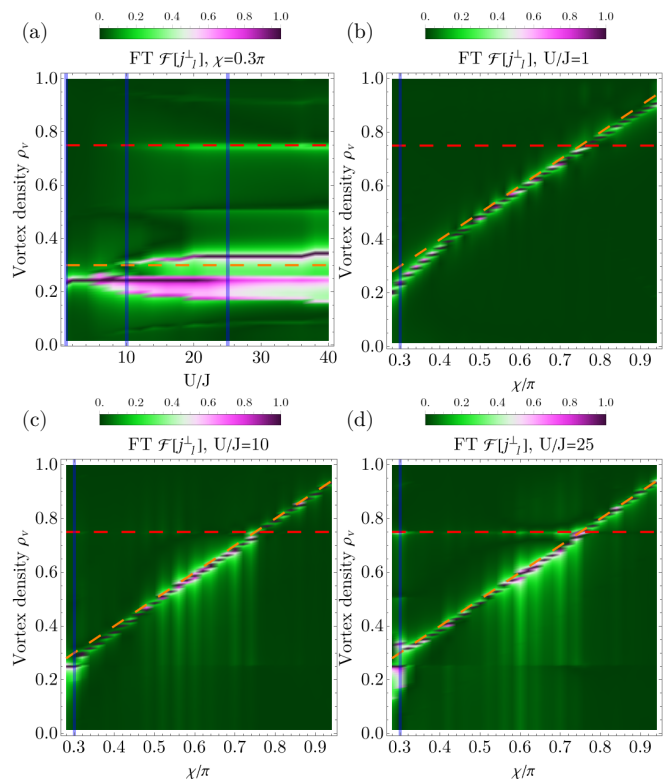


FIG. 22: The Fourier transform of the ground state local rung currents, j_j^{\perp} , as a function of (a) the on-site interactions U/J , (b)-(d) the flux χ for $J_{\parallel}/J = 2$, $\rho = 0.25$ and (a) $\chi = 0.3\pi$, (b) $U/J = 1$, (c) $U/J = 10$, (d) $U/J = 25$. The vertical axis has been scaled in terms of the vortex density ρ_v . The orange dashed lines corresponds to the expectation of the vortex superfluid phase of $\rho_v = \chi/\pi$, the red dashed lines corresponds to the value $\rho_v = 1 - \rho = 0.75$. In the vertical blue lines marks in (a) the interactions strengths used in panels (b)-(d), and in (b)-(d) the values of the flux used in panel (a). The system size used is (a) $L = 90$, (b)-(d) $L = 120$. We normalize the Fourier transform such that its maximum is equal to one for each column.

contrast with our analysis for the large positive $\langle\langle P_H \rangle\rangle$ being correlated to the presence of $\rho_v = 1 - \rho$ appearing at larger values of χ , which we observed for many parameter sets.

VI. DISCUSSIONS AND CONCLUSIONS

To summarize, we have investigated the behavior of the Hall polarization for a triangular Bose-Hubbard ladder in a magnetic field, focusing on the effects of the on-site interactions from the weakly interacting regime to the hardcore limit. We compute the time-evolution of the system following the quench of a linear potential which induces a current through the system, analyzing both the short-time non-equilibrium dynamics of the Hall polarization and its long-time saturation value. We show that the Hall polarization can be employed to fingerprint

and probe many of the features of the underlying ground state phase diagram, being particularly sensitive to the phase boundaries and the interplay of commensurate-incommensurate effects occurring at strong interactions. In the non-interacting limit the equilibrium Hall polarization diverges as we approach the phase transition from the M-SF to the V-SF or BC-SF. Interestingly, this single particle effect can still determine a very strong negative Hall response also in the regimes of strong interactions. Our results also show the possibility of changing the sign of the Hall polarization, for some parameter sets, e.g. large fillings $\rho > 0.5$ and strong interactions, this can be explained by the change of the character of the carries from particles to holes, while for other regimes, e.g. $\rho = 0.25$ in the V-SF and BC-SF, we do not have a similar argument. Sign changes in the Hall response have also previously been linked to the presence of a topological phase transition [54, 55]. We could correlate the strong positive values of the Hall polarization present for strong interactions to the presence of a commensurate vortex density in the otherwise incommensurate vortex

superfluid.

We expect that our work will be experimentally relevant in the near future, as the Hall response has been measured for ultracold fermionic atoms confined to square ladders [19]. Triangular flux ladders have been realized in momentum space in Ref. [56], or could be achieved in real-space by employing optical lattices at the antimagic wavelength [44]. Further motivation is given by the ongoing experimental interest in exploring frustration-driven quantum phenomena with ultracold atoms in triangular geometries [57–63].

ACKNOWLEDGMENTS

We thank J.-S. Bernier, M. Filippone for fruitful discussions. This work was supported by the Swiss National Science Foundation under Division II grant 200020-219400.

-
- [1] A. Kitaev, *Fault-tolerant quantum computation by anyons*, *Annals of Physics* **303**, 2 (2003).
 - [2] C. Nayak, S. H. Simon, A. Stern, M. Freedman, and S. Das Sarma, *Non-Abelian anyons and topological quantum computation*, *Rev. Mod. Phys.* **80**, 1083 (2008).
 - [3] D. C. Tsui, H. L. Stormer, and A. C. Gossard, *Two-Dimensional Magnetotransport in the Extreme Quantum Limit*, *Phys. Rev. Lett.* **48**, 1559 (1982).
 - [4] R. B. Laughlin, *Anomalous Quantum Hall Effect: An Incompressible Quantum Fluid with Fractionally Charged Excitations*, *Phys. Rev. Lett.* **50**, 1395 (1983).
 - [5] H. L. Stormer, D. C. Tsui, and A. C. Gossard, *The fractional quantum Hall effect*, *Rev. Mod. Phys.* **71**, S298 (1999).
 - [6] J. Dalibard, F. Gerbier, G. Juzeliūnas, and P. Öhberg, *Colloquium: Artificial gauge potentials for neutral atoms*, *Rev. Mod. Phys.* **83**, 1523 (2011).
 - [7] N. Goldman, G. Juzeliūnas, P. Öhberg, and I. B. Spielman, *Light-induced gauge fields for ultracold atoms*, *Reports on Progress in Physics* **77**, 126401 (2014).
 - [8] P. Hauke and I. Carusotto, *Quantum Hall and Synthetic Magnetic-Field Effects in Ultra-Cold Atomic Systems* (2022), [arXiv:2206.07727](https://arxiv.org/abs/2206.07727).
 - [9] M. Aidelsburger, M. Atala, S. Nascimbène, S. Trotzky, Y.-A. Chen, and I. Bloch, *Experimental Realization of Strong Effective Magnetic Fields in an Optical Lattice*, *Phys. Rev. Lett.* **107**, 255301 (2011).
 - [10] J. Struck, C. Ölschläger, M. Weinberg, P. Hauke, J. Simonet, A. Eckardt, M. Lewenstein, K. Sengstock, and P. Windpassinger, *Tunable Gauge Potential for Neutral and Spinless Particles in Driven Optical Lattices*, *Phys. Rev. Lett.* **108**, 225304 (2012).
 - [11] M. Aidelsburger, M. Atala, M. Lohse, J. T. Barreiro, B. Paredes, and I. Bloch, *Realization of the Hofstadter Hamiltonian with Ultracold Atoms in Optical Lattices*, *Phys. Rev. Lett.* **111**, 185301 (2013).
 - [12] H. Miyake, G. A. Siviloglou, C. J. Kennedy, W. C. Burton, and W. Ketterle, *Realizing the Harper Hamiltonian with Laser-Assisted Tunneling in Optical Lattices*, *Phys. Rev. Lett.* **111**, 185302 (2013).
 - [13] M. Atala, M. Aidelsburger, M. Lohse, J. T. Barreiro, B. Paredes, and I. Bloch, *Observation of chiral currents with ultracold atoms in bosonic ladders*, *Nature Physics* **10**, 588 (2014).
 - [14] M. Aidelsburger, M. Lohse, C. Schweizer, M. Atala, J. T. Barreiro, S. Nascimbène, N. R. Cooper, I. Bloch, and N. Goldman, *Measuring the Chern number of Hofstadter bands with ultracold bosonic atoms*, *Nature Physics* **11**, 162 (2015).
 - [15] M. Mancini, G. Pagano, G. Cappellini, L. Livi, M. Rider, J. Catani, C. Sias, P. Zoller, M. Inguscio, M. Dalmonte, and L. Fallani, *Observation of chiral edge states with neutral fermions in synthetic Hall ribbons*, *Science* **349**, 1510 (2015).
 - [16] M. E. Tai, A. Lukin, M. Rispoli, R. Schittko, T. Menke, D. Borgnia, P. M. Preiss, F. Grusdt, A. M. Kaufman, and M. Greiner, *Microscopy of the interacting Harper–Hofstadter model in the two-body limit*, *Nature* **546**, 519 (2017).
 - [17] D. Genkina, L. M. Aycok, H.-I. Lu, M. Lu, A. M. Pineiro, and I. B. Spielman, *Imaging topology of Hofstadter ribbons*, *New Journal of Physics* **21**, 053021 (2019).
 - [18] T. Chalopin, T. Satoor, A. Evrard, V. Makhlov, J. Dalibard, R. Lopes, and S. Nascimbene, *Probing chiral edge dynamics and bulk topology of a synthetic Hall system*, *Nature Physics* **16**, 1017 (2020).
 - [19] T.-W. Zhou, G. Cappellini, D. Tusi, L. Franchi, J. Paravicini, C. Repellin, S. Greschner, M. Inguscio, T. Giamarchi, M. Filippone, J. Catani, and L. Fallani, *Observation of universal Hall response in strongly interacting Fermions*, *Science* **381**, 427 (2023).
 - [20] J. Léonard, S. Kim, J. Kwan, P. Segura, F. Grusdt,

- C. Repellin, N. Goldman, and M. Greiner, *Realization of a fractional quantum Hall state with ultracold atoms*, *Nature* **619**, 495 (2023).
- [21] C. Repellin, J. Léonard, and N. Goldman, *Fractional Chern insulators of few bosons in a box: Hall plateaus from center-of-mass drifts and density profiles*, *Phys. Rev. A* **102**, 063316 (2020).
- [22] L. Peralta Gavensky, S. Sachdev, and N. Goldman, *Connecting the Many-Body Chern Number to Luttinger's Theorem through Středa's Formula*, *Phys. Rev. Lett.* **131**, 236601 (2023).
- [23] P. Prelovšek, M. Long, T. Markež, and X. Zotos, *Hall Constant of Strongly Correlated Electrons on a Ladder*, *Phys. Rev. Lett.* **83**, 2785 (1999).
- [24] X. Zotos, F. Naef, M. Long, and P. Prelovšek, *Reactive Hall Response*, *Phys. Rev. Lett.* **85**, 377 (2000).
- [25] S. Greschner, M. Filippone, and T. Giamarchi, *Universal Hall Response in Interacting Quantum Systems*, *Phys. Rev. Lett.* **122**, 083402 (2019).
- [26] M. Buser, S. Greschner, U. Schollwöck, and T. Giamarchi, *Probing the Hall Voltage in Synthetic Quantum Systems*, *Phys. Rev. Lett.* **126**, 030501 (2021).
- [27] R. Citro, T. Giamarchi, and E. Orignac, *Hall response in interacting bosonic and fermionic ladders*, arXiv:2404.16973 (2024), arXiv:2404.16973 .
- [28] C.-M. Halati and T. Giamarchi, *Exploring Frustration Effects of Strongly Interacting Bosons via the Hall Response* (2024), arXiv:2405.19030 .
- [29] A. Lopatin, A. Georges, and T. Giamarchi, *Hall effect and interchain magneto-optical properties of coupled Luttinger liquids*, *Phys. Rev. B* **63**, 075109 (2001).
- [30] G. León, C. Berthod, and T. Giamarchi, *Hall effect in strongly correlated low-dimensional systems*, *Phys. Rev. B* **75**, 195123 (2007).
- [31] A. Auerbach, *Hall Number of Strongly Correlated Metals*, *Phys. Rev. Lett.* **121**, 066601 (2018).
- [32] T. Mishra, R. V. Pai, S. Mukerjee, and A. Paramekanti, *Quantum phases and phase transitions of frustrated hardcore bosons on a triangular ladder*, *Phys. Rev. B* **87**, 174504 (2013).
- [33] E. Anisimovas, M. Račiūnas, C. Sträter, A. Eckardt, I. B. Spielman, and G. Juzeliūnas, *Semisynthetic zigzag optical lattice for ultracold bosons*, *Phys. Rev. A* **94**, 063632 (2016).
- [34] F. A. An, E. J. Meier, and B. Gadway, *Engineering a Flux-Dependent Mobility Edge in Disordered Zigzag Chains*, *Phys. Rev. X* **8**, 031045 (2018).
- [35] C. Romen and A. M. Läuchli, *Chiral Mott insulators in frustrated Bose-Hubbard models on ladders and two-dimensional lattices: A combined perturbative and density matrix renormalization group study*, *Phys. Rev. B* **98**, 054519 (2018).
- [36] S. Greschner and T. Mishra, *Interacting bosons in generalized zigzag and railroad-trestle models*, *Phys. Rev. B* **100**, 144405 (2019).
- [37] J. Cabedo, J. Claramunt, J. Mompant, V. Ahufinger, and A. Celi, *Effective triangular ladders with staggered flux from spin-orbit coupling in 1D optical lattices*, *The European Physical Journal D* **74**, 123 (2020).
- [38] Y. Li, H. Cai, D.-w. Wang, L. Li, J. Yuan, and W. Li, *Many-Body Chiral Edge Currents and Sliding Phases of Atomic Spin Waves in Momentum-Space Lattice*, *Phys. Rev. Lett.* **124**, 140401 (2020).
- [39] S. Singha Roy, L. Carl, and P. Hauke, *Genuine multipartite entanglement in a one-dimensional Bose-Hubbard model with frustrated hopping*, *Phys. Rev. B* **106**, 195158 (2022).
- [40] C.-M. Halati and T. Giamarchi, *Bose-Hubbard triangular ladder in an artificial gauge field*, *Phys. Rev. Res.* **5**, 013126 (2023).
- [41] L. Barbiero, J. Cabedo, M. Lewenstein, L. Tarruell, and A. Celi, *Frustrated magnets without geometrical frustration in bosonic flux ladders*, *Phys. Rev. Res.* **5**, L042008 (2023).
- [42] B. Beradze and A. Nersesyan, *Spectrum, Lifshitz transitions and orbital current in frustrated fermionic ladders with a uniform flux*, *The European Physical Journal B* **96**, 2 (2023).
- [43] B. Beradze, M. Tsitsishvili, E. Tirrito, M. Dalmonte, T. Chanda, and A. Nersesyan, *Emergence of non-Abelian SU(2) invariance in Abelian frustrated fermionic ladders*, *Phys. Rev. B* **108**, 075146 (2023).
- [44] N. Baldelli, C. R. Cabrera, S. Julià-Farré, M. Aidelsburger, and L. Barbiero, *Frustrated Extended Bose-Hubbard Model and Deconfined Quantum Critical Points with Optical Lattices at the Antimagic Wavelength*, *Phys. Rev. Lett.* **132**, 153401 (2024).
- [45] G. León, C. Berthod, T. Giamarchi, and A. J. Millis, *Hall effect on the triangular lattice*, *Phys. Rev. B* **78**, 085105 (2008).
- [46] S. R. White, *Density matrix formulation for quantum renormalization groups*, *Phys. Rev. Lett.* **69**, 2863 (1992).
- [47] U. Schollwöck, *The density-matrix renormalization group*, *Rev. Mod. Phys.* **77**, 259 (2005).
- [48] U. Schollwöck, *The density-matrix renormalization group in the age of matrix product states*, *Annals of Physics* **326**, 96 (2011).
- [49] K. A. Hallberg, *New trends in density matrix renormalization*, *Advances in Physics* **55**, 477 (2006).
- [50] E. Jeckelmann, *Dynamical density-matrix renormalization-group method*, *Phys. Rev. B* **66**, 045114 (2002).
- [51] M. Fishman, S. R. White, and E. M. Stoudenmire, *The ITensor Software Library for Tensor Network Calculations*, *SciPost Phys. Codebases* , 4 (2022).
- [52] A. J. Daley, C. Kollath, U. Schollwöck, and G. Vidal, *Time-dependent density-matrix renormalization-group using adaptive effective Hilbert spaces*, *Journal of Statistical Mechanics: Theory and Experiment* **2004**, P04005 (2004).
- [53] S. R. White and A. E. Feiguin, *Real-Time Evolution Using the Density Matrix Renormalization Group*, *Phys. Rev. Lett.* **93**, 076401 (2004).
- [54] S. D. Huber and N. H. Lindner, *Topological transitions for lattice bosons in a magnetic field*, *Proceedings of the National Academy of Sciences* **108**, 19925 (2011).
- [55] E. Berg, S. D. Huber, and N. H. Lindner, *Sign reversal of the Hall response in a crystalline superconductor*, *Phys. Rev. B* **91**, 024507 (2015).
- [56] Y. Li, H. Du, Y. Wang, J. Liang, L. Xiao, W. Yi, J. Ma, and S. Jia, *Observation of frustrated chiral dynamics in an interacting triangular flux ladder*, *Nature Communications* **14**, 7560 (2023).
- [57] C. Becker, P. Soltan-Panahi, J. Kronjäger, S. Dörscher, K. Bongs, and K. Sengstock, *Ultracold quantum gases in triangular optical lattices*, *New Journal of Physics* **12**, 065025 (2010).

- [58] J. Struck, C. Ölschläger, R. L. Targat, P. Soltan-Panahi, A. Eckardt, M. Lewenstein, P. Windpassinger, and K. Sengstock, *Quantum Simulation of Frustrated Classical Magnetism in Triangular Optical Lattices*, *Science* **333**, 996 (2011).
- [59] J. Yang, L. Liu, J. Mongkolkiattichai, and P. Schauss, *Site-Resolved Imaging of Ultracold Fermions in a Triangular-Lattice Quantum Gas Microscope*, *PRX Quantum* **2**, 020344 (2021).
- [60] J. Mongkolkiattichai, L. Liu, D. Garwood, J. Yang, and P. Schauss, *Quantum gas microscopy of fermionic triangular-lattice Mott insulators*, *Phys. Rev. A* **108**, L061301 (2023).
- [61] M. Xu, L. H. Kendrick, A. Kale, Y. Gang, G. Ji, R. T. Scalettar, M. Lebrat, and M. Greiner, *Frustration- and doping-induced magnetism in a Fermi–Hubbard simulator*, *Nature* **620**, 971 (2023).
- [62] M. Lebrat, M. Xu, L. H. Kendrick, A. Kale, Y. Gang, P. Seetharaman, I. Morera, E. Khatami, E. Demler, and M. Greiner, *Observation of Nagaoka polarons in a Fermi–Hubbard quantum simulator*, *Nature* **629**, 317 (2024).
- [63] M. L. Prichard, B. M. Spar, I. Morera, E. Demler, Z. Z. Yan, and W. S. Bakr, *Directly imaging spin polarons in a kinetically frustrated Hubbard system*, *Nature* **629**, 323 (2024).